

Fast Bayesian Functional Principal Components Analysis

Joseph Sartini ^{*1}, Xinkai Zhou¹, Liz Selvin², Scott Zeger¹, and Ciprian M. Crainiceanu¹

¹Department of Biostatistics, Johns Hopkins University

²Department of Epidemiology, Johns Hopkins University

December 25, 2024

Abstract

Functional Principal Components Analysis (FPCA) is one of the most successful and widely used analytic tools for exploration and dimension reduction of functional data. Standard implementations of FPCA estimate the principal components from the data but ignore their sampling variability in subsequent inferences. To address this problem, we propose the Fast Bayesian Functional Principal Components Analysis (Fast BayesFPCA), that treats principal components as parameters on the Stiefel manifold. To ensure efficiency, stability, and scalability we introduce three innovations: (1) project all eigenfunctions onto an orthonormal spline basis, reducing modeling considerations to a smaller-dimensional Stiefel manifold; (2) induce a uniform prior on the Stiefel manifold of the principal component spline coefficients via the polar representation of a matrix with entries following independent standard Normal priors; and (3) constrain sampling using the assumed FPCA structure to improve stability. We demonstrate the application of Fast BayesFPCA to characterize the variability in mealtime glucose from the Dietary Approaches to Stop Hypertension for Diabetes Continuous Glucose Monitoring (DASH4D CGM) study. All relevant STAN code and simulation routines are available as supplementary material.

Keywords: Bayesian Methods, Functional Data, Computationally Intensive Methods, Uncertainty Quantification, Semiparametric Methods

^{*}DASH4D Trial is funded by a grant from the Sheikh Khalifa Stroke Institute at Johns Hopkins University School of Medicine. The DASH4D-CGM study is funded by NIH/NIDDK grant R01 DK128900. Dr. Selvin was also supported by NIH/NHLBI grant K24 HL152440. Mr. Sartini was supported by Grant Number T32 HL007024 from the National Heart, Lung, and Blood Institute, National Institutes of Health. The content is solely the responsibility of the authors and does not necessarily represent the official views of the National Institutes of Health. Abbott Diabetes Care provided continuous glucose monitoring systems for this investigator-initiated research.

1 Introduction

Functional principal component analysis is a first line analytic approach in high-dimensional applications where the data are sampled over a continuous domain. The standard implementation relies on diagonalizing a smooth estimator of the covariance operator using the observed data, followed by inference conditional on the functional principal components (FPCs) [6]. This assumes that the FPCs do not have sampling variability, which is easy to invalidate by simply resampling the data. Whether this assumption affects downstream inferences remains an open question and requires further analyses.

We propose a model where the FPCs are treated as random variables. Because the eigenfunctions are orthonormal, their natural parameter space is the Stiefel manifold, the space of matrices with orthonormal columns. We design a Bayesian algorithm to efficiently sample this parameter space using a novel combination of three techniques: (1) project all eigenfunctions onto an orthonormal spline basis to reduce dimensionality - the coefficient matrix will lie on a lower dimensional Stiefel manifold if and only if the principal components lie on a higher dimensional Stiefel manifold; (2) induce a uniform prior on the Stiefel manifold of the FPC spline coefficients, representing a subspace of smooth functions at the original data scale, using the polar decomposition; and (3) leverage ordered objects in STAN and reasonable sampling initialization. These elements together produce a fast, stable, and scalable algorithm easily implemented in reproducible software.

Fast BayesFPCA is part of an expanding literature modeling FPCs on the Stiefel manifold. One of the first attempts implemented robust likelihood optimization adapted to the manifold geometry [25], but did not account for uncertainty in the eigenfunctions. A fully Bayesian implementation of FPCA was proposed in [14] using spline expansion to smooth functional components and post-processing to obtain the relevant posterior distributions. More recently, [18] modeled the data using the Singular Value Decomposition (SVD) on the original data space, combined with polar decomposition and matrix normal priors to induce orthonormality and smoothness of the FPCs in the original data space. This method is related to Fast BayesFPCA; however, it models the higher dimensional Stiefel manifold of eigenfunctions on the original space rather than the lower dimensional Stiefel manifold of spline coefficients. An approach related to that of [18] was recently proposed [34], though it used splines to model the FPCs and Gibbs sampling to simulate the posterior. At the time of writing this paper, no software is available for this approach. Another very recent contribution [23] proposed an extensible variational Bayes approach to FPCA and provided supporting software. Fast BayesFPCA leverages the dimensionality reduction of FPCA, the low rank spline representation of the FPCs, and the mixed effects model structure associated with smoothing penalties to provide a scalable and stable alternative to existing methods.

This research is motivated by a study goal of the Dietary Approaches to Stop Hyperten-

sion for Diabetes Continuous Glucose Monitoring (DASH4D CGM) clinical trial. DASH4D CGM was a crossover feeding trial which collected meal timing data for a subset of 65 participants, producing a total of 768 meals divided among 4 diets. For the purposes of distributing meals and collecting biomarker data, participants visited the study site and ate meals there 3 times per week. Study staff recorded the start times for these meals when possible. We evaluated mealtime (pre- and postprandial) responses using CGM data collected during the observed mealtimes. It is crucial to characterize these responses, as postprandial glucose is an important marker of metabolic insulin responsiveness known to be associated with adverse cardiovascular outcomes [12, 16].

Analyses of postprandial CGM glucose with verified mealtimes are rare, and previous studies do not consider functional responses [1, 27]. We address this gap by examining five-hour CGM curves beginning one hour before and ending four hours after each meal. As the main results of the trial are not yet published, this paper characterizes the variability of observed curves by diet, rather than the treatment effects. We apply FPCA to the CGM curves aggregated by participant and Multilevel FPCA (MFPCA) to the individual meal responses within each diet. The number of participants in this study is relatively small because of data collection costs. Therefore, the estimated FPCs could have substantial variability, potentially impacting downstream analyses. We propose to quantify this variability to understand its potential effect on statistical inferences of interest.

The rest of the paper is organized as follows. Section 2 presents the model and full conditionals for Fast BayesFPCA. Section 3 provides the `STAN` code. Section 4 compares Fast BayesFPCA with existing implementations [14, 18] in two simulation scenarios. Section 5 details the results of applying Fast BayesFPCA to the motivating data from the DASH4D clinical trial. Section 6 provides a short discussion.

2 Methods

The data structure is of the form $Y_i(t), i = 1, \dots, N, t \in \{t_1, \dots, t_M\} \in [0, 1]$, though this could easily be generalized to other domains (e.g., space). Below we describe the model structure, priors, and full conditionals for Fast BayesFPCA.

2.1 Conditional likelihood

The Gaussian FPCA model is

$$Y_i(t) = \mu(t) + \sum_{k=1}^{\infty} \xi_{ik} \phi_k(t) + \epsilon_i(t) \approx \mu(t) + \sum_{k=1}^K \xi_{ik} \phi_k(t) + \epsilon_i(t), \quad (1)$$

where $\mu(t)$ is the population mean, $\phi_k(t)$, $k = 1, \dots, K$, are orthonormal eigenfunctions of the covariance operator of $Y_i(t)$, $\xi_{ik} \sim N(0, \lambda_k)$, λ_k are the eigenvalues corresponding

to $\phi_k(t)$, $\epsilon_i(t) \sim N(0, \sigma^2)$ is the error process, and $\epsilon_i(t)$ and ξ_{ik} are mutually independent over i and k . For the purpose of this paper, the number of principal components, K , is fixed. The model can and will be expanded, but we use this initial formulation to build the essential machinery for a wide variety of related models.

Model (1) is a first line approach to analysis of high dimensional data [7] because in many applications $K \ll M$ and model (1) provides a low-dimensional approximation to the original high-dimensional data. Moreover, conditional on the FPCs, $\phi_k(\cdot)$, the model is a simple Gaussian random effects model. Here we consider the case when the $\phi_k(t)$ are concurrently estimated from the data with their own associated uncertainty. We will show that all full conditionals in the associated Bayesian model are straightforward to simulate except for those of $\phi_k(\cdot)$. *The difficulty lies in simulating from this distribution in a way that is efficient, scalable and stable across simulations and applications.*

2.2 Priors

We expand both the mean function and eigenfunctions using the same orthonormal spline basis, which can be derived by orthogonalizing any spline basis. Let \mathbf{B} be the $M \times Q$ matrix representation of the Q dimensional orthonormal spline basis, where $Q \geq K$. Each column of \mathbf{B} corresponds to a spline basis and each row corresponds to a sampling point. Because we use an orthonormal spline basis, $\mathbf{B}^t\mathbf{B} = I_Q$, the identity matrix of dimension Q . If $\mu = \{\mu(t_1), \dots, \mu(t_M)\}^t$ and $\phi_k = \{\phi_k(t_1), \dots, \phi_k(t_M)\}^t$ are M -dimensional vectors, the spline expansions have the form $\mu = \mathbf{B}w_\mu$ and $\phi_k = \mathbf{B}\psi_k$, where w_μ , and ψ_k are Q -dimensional vectors of spline coefficients.

Denote by $\Phi = [\phi_1 | \dots | \phi_K]$ the $M \times K$ dimensional matrix obtained by column binding the vectors ϕ_k and by $\Psi = [\psi_1 | \dots | \psi_K]$ the $Q \times K$ dimensional matrix of parameters obtained by column binding the vectors ψ_k . As $\Phi = \mathbf{B}\Psi$, it follows that $\Phi^t\Phi = \Psi^t\mathbf{B}^t\mathbf{B}\Psi = \Psi^t\Psi$ because, by construction, $\mathbf{B}^t\mathbf{B} = I_Q$. Therefore, $\Phi^t\Phi = \Psi^t\Psi$, implying that the eigenfunctions on the original high-dimensional space of the data, ϕ_k , are orthonormal if and only if the vectors of parameters in the low dimensional space of spline coefficients, ψ_k , are orthonormal. We thus reduce the problem of sampling M -dimensional orthonormal FPCs to one of sampling Q -dimensional parameters of an orthonormal spline basis. This has substantial implications on Fast BayesFPCA's performance.

We add smoothing priors for both the mean $\mu(t)$ and eigenfunctions $\phi_k(t)$ using posterior penalties of the type $\alpha \int f^2(t)dt + (1 - \alpha) \int \{f''(t)\}^2dt$, where $f(\cdot)$ denotes a generic function. This penalty, used in [14], contains the fixed weighting parameter α , where $\alpha = 0$ corresponds to the famous penalized spline prior [8, 24]. If $f(t) \approx B(t)\theta$, then the penalty is a quadratic form of θ with associated matrix \mathbf{P}_α . See Supplement Section S1 for derivation of \mathbf{P}_α . We use $\alpha = 0.1$ for consistency with existing implementations, but Fast BayesFPCA can handle any α , including $\alpha = 0$. This quadratic penalization is akin to assuming Normal

priors for the mean and FPC spline parameters, respectively [2, 26, 32]

$$w_\mu \propto \exp \left\{ -\frac{h_\mu}{2\sigma^2} w_\mu^t \mathbf{P}_\alpha w_\mu \right\}, \quad \psi_k \propto \exp \left\{ -\frac{h_k}{2\sigma^2} \psi_k^t \mathbf{P}_\alpha \psi_k \right\},$$

where $h_\mu > 0$ and $h_k > 0$ are different smoothing parameters. Though this could be simplified by assuming the same smoothing parameter across FPCs, we do not simplify here.

We assume that the inverse variance components and smoothing parameters (which can be viewed as inverse variance components) have Gamma priors: $1/\sigma^2 \sim \Gamma(\alpha_\sigma, \beta_\sigma)$, $1/\lambda_k \sim \Gamma(\alpha_\lambda, \beta_\lambda)$, $h_k \sim \Gamma(\alpha_\psi, \beta_\psi)$, for $k = 1, \dots, K$, and $h_\mu \sim \Gamma(\alpha_\mu, \beta_\mu)$, where $\Gamma(a, b)$ denotes the Gamma distribution with mean a/b and variance a/b^2 . For details on specific choices of these priors, see the STAN [3] implementation in Section 3. For a discussion on the choice of Gamma priors for inverse variance components, see [5, 6].

Recall that the $Q \times K$ dimensional matrix Ψ has orthonormal columns if and only if the functions $\phi_k(\cdot)$ are orthonormal. The space of $Q \times K$ dimensional matrices with orthonormal columns is called the Stiefel manifold [17], which has a finite volume. We denote this space $\mathcal{V}_{Q,K}$ and assume a uniform prior on this space [21] proportional to $\mathbb{1}(\Psi \in \mathcal{V}_{Q,K})$. At the data level, this induces a uniform prior on the intersection $\text{span}(\mathbf{B}) \cap \mathcal{V}_{M,K}$.

2.3 Posterior and full conditionals

Given the conditional likelihood detailed in Section 2.1 and priors described in Section 2.2 the posterior likelihood $[\Theta|Y]$ of all model parameters Θ given data Y is proportional to

$$\begin{aligned} & \prod_{i=1}^N \prod_{m=1}^M N\{Y_i(t_m) | (Bw_\mu)_m + \sum_{k=1}^K \xi_{ik} (B\psi_k)_m, \sigma^2\} \times \Gamma^{-1}(\sigma^2 | \alpha_\sigma, \beta_\sigma) \\ & \times \left\{ \prod_{k=1}^K N(\xi_{ik} | 0, \lambda_k) \times \Gamma^{-1}(\lambda_k | \alpha_\lambda, \beta_\lambda) \times \exp \left(-\frac{h_k}{2\sigma^2} \psi_k^t \mathbf{P}_\alpha \psi_k \right) \times \Gamma(h_k | \alpha_\psi, \beta_\psi) \right\} \quad (2) \\ & \times \exp \left(-\frac{h_\mu}{2\sigma^2} w_\mu^t \mathbf{P}_\alpha w_\mu \right) \times \Gamma(h_\mu | \alpha_\mu, \beta_\mu) \times \mathbb{1}(\Psi \in \mathcal{V}_{Q,K}) \end{aligned}$$

Result 1. *The full conditionals of the scores, ξ_{ik} , and mean function parameters, w_μ , are normal. The full conditionals of the inverse eigenvalues, $1/\lambda_k$, inverse noise variance, $1/\sigma^2$, and the smoothing parameters h_μ , h_k for $k = 1, \dots, K$ have Gamma distributions. These distributions are provided in Supplement Section S2, with the exception of the full conditionals for the scores*

$$[\xi_{ik} | \text{others}] \sim N \left\{ \frac{\lambda_k (Y_i - \mathbf{B}w_\mu)^t \mathbf{B}\psi_k}{\lambda_k + \sigma^2}, \frac{\lambda_k \sigma^2}{\lambda_k + \sigma^2} \right\},$$

where $Y_i = \{Y_i(t_1), \dots, Y_i(t_M)\}^t$ is the M -dimensional vector of observations for participant i .

Result 2. *The full conditional of the eigenfunction matrix Ψ has the generalized Bingham-Von Mises-Fisher (BMF) distribution*

$$[\Psi | \text{others}] \propto \exp \left[\text{tr} \left\{ -\frac{\Psi^t \mathbf{H} \Psi^t}{2\sigma^2} + \frac{\Xi^t (\mathbf{Y} - \mathbf{1}_N \otimes w_\mu^t \mathbf{B}^t) \mathbf{B} \Psi}{\sigma^2} \right\} \right] \mathbb{1}(\Psi \in \mathcal{V}_{Q,K}),$$

where $\mathbf{H} = \text{diag}(h_1, \dots, h_K)$, Ξ is a $N \times K$ dimensional matrix with the (i, k) entry equal to $\xi_{i,k}$, and the matrix \mathbf{Y} is the $N \times M$ dimensional matrix with the row i equal to Y_i^t . The quantity $\mathbf{1}_N$ is the N -dimensional column vector of ones, the symbol \otimes denotes the Kronecker product of matrices, and “tr” denotes the trace of a matrix.

2.4 The polar decomposition

We will sample from the non-standard conditional distribution of Ψ indirectly, by inducing a uniform prior on $\mathcal{V}_{Q,K}$. To that end, we introduce the polar decomposition of a $Q \times K$ matrix \mathbf{X} : $\mathbf{X} = \Psi \mathbf{P}$, where $\Psi \in \mathbb{R}^{Q \times K}$ is orthonormal and $\mathbf{P} \in \mathbb{R}^{K \times K}$ is positive semi-definite. Note that Ψ is on the Stiefel manifold by construction and is a deterministic function of \mathbf{X} up to the choice of algorithm. Crucially, if \mathbf{X} has independent $N(0, 1)$ entries, then Ψ is uniformly distributed on the Stiefel manifold [4]. Therefore, if the entries of \mathbf{X} are random variables with independent $N(0, 1)$ priors, then the posterior of Ψ is the posterior distribution described in Result 2. Householder reflections or Givens rotations [19, 28] could also be used to induced uniform priors on the Stiefel manifold, but we focus on the simple and familiar polar decomposition.

There are multiple ways to obtain a polar decomposition, but here we use the eigen-decomposition of $\mathbf{X}^t \mathbf{X} = \mathbf{Z} \mathbf{D} \mathbf{Z}^t$ and define $\Psi = \mathbf{X} \mathbf{Z} \mathbf{D}^{-1/2} \mathbf{Z}^t$ and $\mathbf{P} = \Psi^t \mathbf{X}$; it can be easily verified that $\Psi^t \Psi = I_Q$. Using this decomposition to sample Ψ works well because: (1) independent $N(0, 1)$ priors on the entries of \mathbf{X} , which induce the uniform prior on Ψ , are computationally simple; (2) the matrix $\mathbf{X} \in \mathbb{R}^{Q \times K}$ is much smaller dimensional than matrix of eigenfunctions $\Phi \in \mathbb{R}^{M \times K}$ where $Q \ll M$; and (3) deterministically calculating Φ from \mathbf{X} can be accomplished efficiently using linear algebra routines, such as those implemented in STAN.

2.5 Extensions

Fast BayesFPCA can be extended to the multilevel, structural, and longitudinal functional data [9, 15, 29], which are becoming increasingly common in applications. We demonstrate how to extend Fast BayesFPCA to fit a multilevel model. The data structure is of the form

$Y_{ij}(t), i = 1, \dots, N, j = 1, \dots, J_i, t \in T = \{t_1, \dots, t_M\}$, where there are J_i observations for each group $i \leq I$. A model for such data is Gaussian MFPCA [9, 35].

$$Y_{ij}(t) = \mu(t) + \eta_j(t) + \sum_{k=1}^{K_1} \xi_{ik} \phi_k^{(1)}(t) + \sum_{l=1}^{K_2} \zeta_{ijl} \phi_l^{(2)}(t) + \epsilon_{ij}(t). \quad (3)$$

where $\mu(t)$ is the population mean and $\eta_j(t)$ are visit-specific deviations from the population mean. The subject-level (level 1) deviations from the visit-specific mean are modeled by $U_i(t) = \sum_{k=1}^{K_1} \xi_{ik} \phi_k^{(1)}(t)$, where $\phi_k^{(1)}(t), k = 1, \dots, K_1$ are the first level eigenfunctions, $\xi_{ik} \sim N(0, \lambda_k^{(1)})$, and $\lambda_k^{(1)}$ are the eigenvalues corresponding to $\phi_k^{(1)}(t)$. The subject/visit-specific (level 2) deviations from the subject-specific mean are modeled by $W_{ij}(t) = \sum_{l=1}^{K_2} \zeta_{ijl} \phi_l^{(2)}(t)$, where $\phi_l^{(2)}(t), l = 1, \dots, K_2$ are the second level eigenfunctions, $\zeta_{ijl} \sim N(0, \lambda_l^{(2)})$, and $\lambda_l^{(2)}$ are the eigenvalues corresponding to $\phi_l^{(2)}(t)$. Finally, $\epsilon_{ij}(t) \sim N(0, \sigma^2)$ is the error process. All functional components, $\epsilon_{ij}(t), U_i(t)$ and $W_{ij}(t)$, are assumed to be mutually independent.

The population mean $\mu(t)$ and the visit-specific deviations $\eta_j(t)$ are modeled using penalized splines. The subject-specific $U_i(t) = \sum_{k=1}^{K_1} \xi_{ik} \phi_k^{(1)}(t)$ and the visit-specific $W_{ij}(t) = \sum_{l=1}^{K_2} \zeta_{ijl} \phi_l^{(2)}(t)$ can be modeled separately using the same techniques described in Sections 2.2, 2.3, and 2.4. Note that this is the first implementation of a Bayesian MFPCA that explicitly models the FPCs.

3 Bayesian implementation in STAN

In this section, we provide the STAN [3] implementation of Fast BayesFPCA, illustrating the algorithm’s simplicity and flexibility.

This `data` section declares constants and imports the data, spline basis, and penalty matrix. All notation is as used in the text.

```
data{
  int N; // Number of time series
  int M; // Number of observations
  int Q; // Number of spline bases
  int K; // Number of Eigenfunctions

  matrix[N, M] Y; // Functional data
  matrix[M, Q] B; // Orthogonal spline basis
  matrix[Q, Q] P; // Penalty matrix for splines
}
```

In the `parameters` block, we model the matrix \mathbf{X} (`X`) rather than $\mathbf{\Psi}$, which will be obtained from \mathbf{X} via the polar decomposition. This block also contains the eigenvalues λ_k (`lambda`) stored using a `positive_ordered` type, which enforces soft ordering of the eigenvalues and corresponding eigenfunctions. The matrix `Scores` is the $N \times K$ score matrix Ξ introduced in Result 2, with (i, k) entry equal to ξ_{ik} .

```

parameters{
  real<lower=0> sigma2; // Error in observation

  // Mean structure
  vector[Q] w_mu; // Population mean parameters
  real<lower=0> h_mu; // Population mean smoothing parameter

  // Covariance structure
  positive_ordered[K] lambda; // Eigenvalues
  vector<lower=0>[K] H; // EF smoothing parameters
  matrix[Q, K] X; // Unconstrained EF weights (X)
  matrix[N, K] Scores; // EF scores (xi)
}

```

The transformed parameters section contains parameters that can be represented as deterministic functions of the data and model parameters. The key component of this block is the definition of Ψ (Psi), which is part of the polar decomposition of the matrix $\mathbf{X} = \Psi\mathbf{P}$. More precisely, $\Psi = \mathbf{XZD}^{-1/2}\mathbf{Z}^t$, where \mathbf{Z} (evec_XtX) is the $K \times K$ dimensional matrix of eigenvectors of $\mathbf{X}^t\mathbf{X}$ and \mathbf{D} (diag(eval_XtX)) is a diagonal matrix containing the corresponding K eigenvalues. Because \mathbf{X} is low dimensional, all these operations are very fast. As shown in simulations, this substantially reduces computation times.

```

// Calculate observed parameters from latent
transformed parameters{
  // Population mean
  vector[M] mu = B * w_mu;

  // Eigenvalues
  vector[K] eval = reverse(lambda);

  // Polar decomposition
  matrix[Q,K] Psi;
  {
    matrix[K,K] evec_XtX = eigenvectors_sym(X'*X);
    vector[K] eval_XtX = eigenvalues_sym(X'*X);
    Psi = X*evec_XtX*diag_matrix(1/sqrt(eval_XtX))*evec_XtX';
  }
}

```

The code proceeds with the specification of priors within the model section. The smoothing parameters h_μ (h_mu) and h_k , $k = 1, \dots, K$ (H) are assigned independent Gamma priors. The eigenvalues λ_k , $k = 1, \dots, K$ (lambda) and the error variance σ^2 (sigma2) have independent inverse Gamma priors. Smoothing priors on the population mean, $\mu(t)$, and eigenfunctions, $\phi_k(t)$, are implemented via quadratic penalties on their coefficients; see Section 2.2 for more details.

The next component is the crucial prior on Ψ (Psi), which just requires specifying independent $N(0, 1)$ priors for each entry of the matrix \mathbf{X} (X). Combined with the definition

of Ψ in the transformed parameters block, this induces a uniform prior on Ψ over the Stiefel manifold. This means that we model the small-dimensional $Q \times K$ matrix \mathbf{X} , constrained by the size of the spline basis and number of eigenfunctions. Because \mathbf{X} is low dimensional, it is much easier to sample than the matrix of eigenfunctions on the original space, which likely contributes to the much improved computational efficiency.

```

model{
  // (Inverse) variance priors
  H ~ gamma(1, 0.005);
  h_mu ~ gamma(1, 0.005);
  lambda ~ inv_gamma(0.1,0.001);
  sigma2 ~ inv_gamma(1,0.001);

  // Smoothing additions to the target density
  target += -(1 * h_mu)/(2 * sigma2) * w_mu' * P * w_mu;
  for(i in 1:K){
    target += -(1 * H[i])/(2 * sigma2) * Psi[,i]' * P * Psi[,i];
  }

  // Indirect uniform prior on Stiefel manifold
  to_vector(X) ~ normal(0,1);

  // FPCA-based Score priors
  for(i in 1:K){
    to_vector(Scores[,i]) ~ normal(0, sqrt(eval[i]));
  }
  :
}

```

We next present the likelihood contributions. This second portion of the `model` block first computes the random deviations $\theta_i(t) = \sum_{k=1}^K \xi_{ik} \phi_k(t) = \sum_{k=1}^K \xi_{ik} \{\mathbf{B}(t)\psi_k\}$. If Θ is the $N \times M$ dimensional matrix with (i, m) entry equal to $\theta_i(t_m)$, it can be shown that $\Theta = \Xi(\mathbf{B}\Psi)^t$. We denote Θ as `Theta` in the code. This value is computed once for each sample and is not saved to conserve memory. The model finally incorporates the observed data contribution in terms of M -dimensional vectors of observations $\mathbf{Y}_i = \{Y_i(t_1), \dots, Y_i(t_m)\}^t$ for all study participants i . Recall from Section 2.1 that FPCA assumes $Y_i(t_m) \sim N\{\mu(t_m) + \theta_i(t_m), \sigma^2\}$, where $\theta_i(t_m) = \sum_{k=1}^K \xi_{ik} \{\mathbf{B}(t)\psi_k\}$.

```

model{
  :
  { // Data Likelihood
    matrix[N,M] Theta = Scores * (B * Psi)'; // Calculate linear predictors
    for(i in 1:N){
      Y[i,] ~ normal(mu + to_vector(Theta[i,]), sqrt(sigma2));
    }
  }
}

```

We present the simplest Bayesian FPCA, though Fast BayesFPCA extends to more complex scenarios. For example, for MFPCA, we construct the spline coefficient matrices Ψ_1 and Ψ_2 instead of just Ψ . For each matrix, we independently model a latent matrix: \mathbf{X}_1 for Ψ_1 and \mathbf{X}_2 for Ψ_2 . We assign independent $N(0, 1)$ priors to the entries of both \mathbf{X}_1 and \mathbf{X}_2 . The Ψ_1 and Ψ_2 matrices are obtained via polar decompositions in `transformed parameters` using the same approach described in Section 2.4. All other components of the model implementation are straightforward, but require careful accounting of indices. We present both the implementation and simulation evaluation of this approach in the Supplement Section S3.3.

4 Simulations

We consider two simulation scenarios for model (1), one built using the Legendre polynomials (denoted by $f_k(\cdot)$) and the other using Fourier bases:

Scenario 1. (S1)

$$\phi_k(t) = \left\{ \frac{1}{\sqrt{M}} f_0(t), \sqrt{\frac{84}{31M}} [f_1(t) - 0.5f_3(t)], -\sqrt{\frac{5}{M}} f_2(t) \right\};$$

$$\lambda_k = \{45000, 7000, 2000\}; \quad \sigma^2 = 4; \quad \mu(t) = 140 - 10f_2(t)$$

Scenario 2. (S2)

$$\phi_k(t) = \left\{ \sqrt{\frac{1}{3M}} [1 - 2\cos(2\pi t)], \sqrt{\frac{1}{15M}} [5\sin(2\pi t) - \sin(4\pi t) - 2\cos(2\pi t)] \right\}$$

$$\lambda_k = \{25000, 8500\}; \quad \sigma^2 = 121; \quad \mu(t) = 10 - 5\sin(2\pi t) - 5\cos(2\pi t)$$

Both scenarios are designed to mimic real data analyses: S1 is meant to emulate the aggregated CGM data described in Section 5, while S2 is based on the physical activity data from wrist-worn accelerometry described and analyzed in [7]. The second data set is not analyzed in this paper, but provides a realistic scenario using publicly available data. A comparison of these scenarios and their corresponding estimates from the DASH4D and NHANES data is presented in the Supplemental Figure S1. All code for performing simulations is publicly available; link provided in the supplement.

For each scenario we generate 100 datasets with $N = 50$ functions observed at $M = 30$ equally spaced points in $[0, 1]$. Fast BayesFPCA (“FAST”) is compared to the Generalized Function-on-Scalar Regression of Goldsmith et al., 2015 [14] (labeled “GFSR”) and polar expansion in the observed data space [18] (labeled “SVD-GP” to capture the combination of SVD transformation paired with the Gaussian Process prior on the eigenfunctions). We do not compare with the methods in [23, 34] because softwares for posterior inference were not available at the time of this simulation. Because the SVD-GP implementation does not include mean estimation, we extend the model to include a mean, $\mu(t)$, which was modeled as a Gaussian Process with smoothing prior.

While the FAST and SVD-GP models sample all FPCA model components, GFSR samples the smooth functions $\mu(t)$ and $\theta_i(t) = \sum_{k=1}^K \xi_{ik} \phi_k(t)$. To obtain the corresponding eigenfunctions, we apply SVD to the $\hat{\theta}_i(t)$ samples, take the right singular vectors, and use GAM to project $Y_i(t) - \hat{\mu}(t)$ onto the eigenfunctions to obtain the corresponding scores.

For all three methods, we aligned the eigenfunction samples to maximize correlation with the first posterior sample; for simulation purposes, they could also be aligned to the real eigenfunctions, as well. Note that eigenfunctions are in $\mathbb{R}^{M \times K}$, and the posterior means may not maintain strict orthonormality. Therefore, for FAST and SVD-GP we calculated the pointwise Euclidean mean of the eigenfunction samples and projected them onto the corresponding Stiefel Manifold. GFRS takes the right singular vectors from the SVD of the mean smooth matrix, which provides estimates on the Stiefel manifold [14].

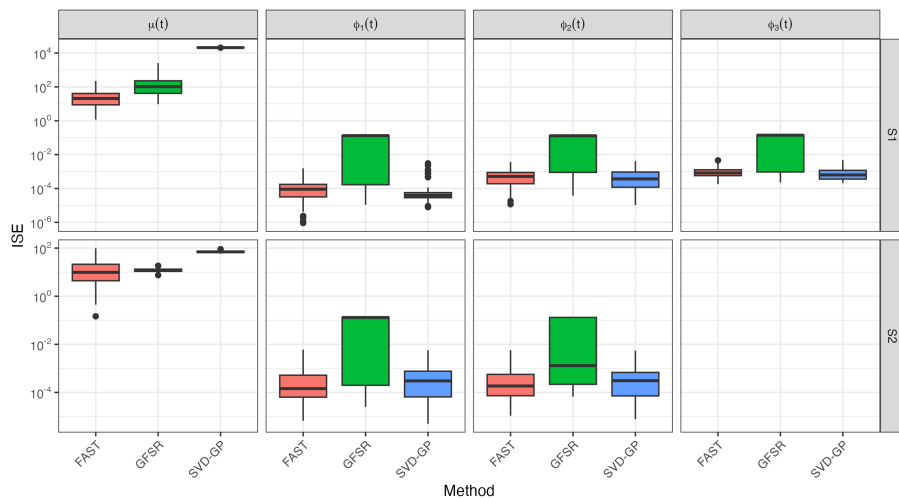


Figure 1: Boxplots of the ISE for the mean and eigenfunctions for FAST (red), GFSR (green), and SVD-GP (blue). First row: S1; second row: S2. Each column: mean or corresponding eigenfunction. Y-axis is on the log scale for presentation purposes.

We first focus on the Integrated Square Error for the mean, $\mu(t)$ and principal components $\phi_k(t)$, evaluated at the time points t_m , $m = 1, \dots, M$. For example, if $\hat{\mu}^b(t)$ is the posterior mean of $\mu(t)$ conditional on the simulated data set $b = 1, \dots, B$, the Integrated

Square Error (ISE) is defined as:

$$\text{ISE}^b\{\mu(\cdot)\} = \frac{1}{M} \sum_{m=1}^M \{\hat{\mu}^b(t_m) - \mu(t_m)\}^2.$$

Combining these values over simulations provide a B -dimensional vector for each method. Similar definitions apply to principal components.

Figure 1 displays the boxplots of the ISE distributions for the mean (first column) and principal components (second to fourth columns) for scenario S1 (first row) and scenario S2 (second row). Boxplots are shown for FAST in red, for GFSR in green, and for SVD-GP in blue. The y-axis in every plot is on the log scale for presentation purposes, as the eigenfunctions are on a different scale from the mean function. FAST has an ISE performance that is either comparable or superior to the other two methods for all functional components; GFSR exhibits consistently larger ISE, which may be due to posterior distribution problems when estimating both fixed (mean) and random effects (covariance) with similar structures. To mitigate this problem, FAST starts sampling in the neighborhood of reasonable $\mu(t)$ and λ_i estimates.

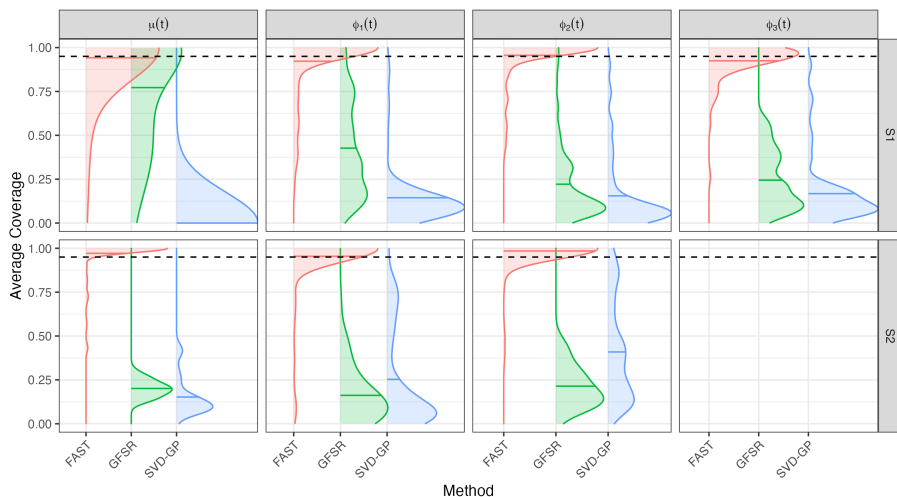


Figure 2: Kernel smoother of coverage probabilities of 95% credible intervals of the true mean and eigenfunctions for FPCA (red), GFSR (green), and SVD-GP (blue). First row: S1; second row: S2. Each column: corresponding function. Distribution means: horizontal solid lines; nominal 95% level: horizontal dotted lines.

We also calculate the posterior coverage probabilities for the true mean $\mu(t)$ and eigenfunctions $\phi_k(t)$, $k = 1, \dots, K$. For each simulated data set $b = 1, \dots, B$, we obtain the equal-tail 95% credible intervals at all time points t_m , $m = 1, \dots, M$ along the domain $[0, 1]$. The proportion of times these credible intervals cover the true function is calculated over t_m for each combination of b and k . These proportions are then collected in a vector of length $B = 100$ for each function $\mu(t), \phi_k(t)$. Figure 2 displays the kernel smooth of

these vectors of proportions for the mean and eigenfunction estimates produced by FPCA (red), GFSR (green), and SVD-GP (blue). The first row corresponds to S1, and the second presents results for S2. FAST has superior, or closer to nominal, coverage probabilities compared to both GFSR and SVD-GP for these functions.

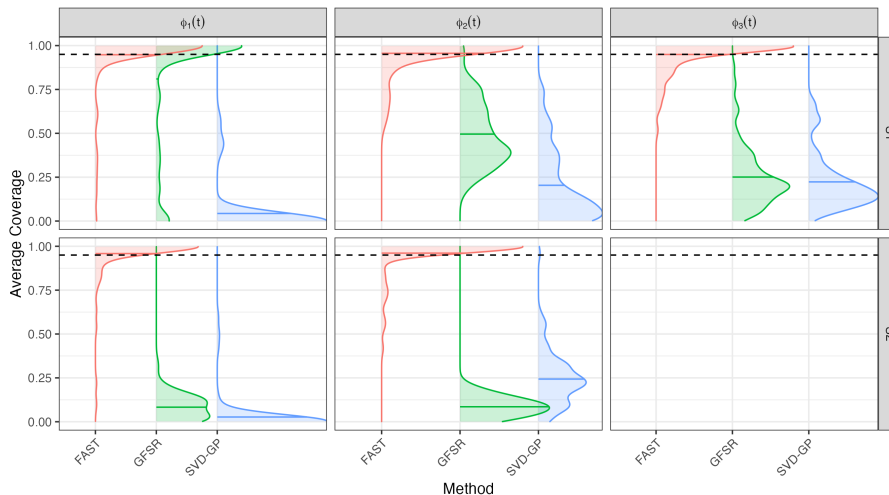


Figure 3: Kernel smoother of coverage probabilities of 95% credible intervals of the true scores, ξ_{ik}^b , for FAST (red), GFSR (green), and SVD-GP (blue). First row: S1; second row: S2. Each column: corresponding eigenfunction. Distribution means: horizontal solid lines; nominal 95% level: horizontal dotted lines.

For each combination of dataset, b , and FPC, k , there are $N = 50$ scores ξ_{ik}^b . For each such combination of b and k , we calculate the proportion of times the equal-tail 95% credible intervals cover the corresponding true scores. These proportions are collected in a vector of length $B = 100$ for each FPC. Figure 3 displays the kernel smooth of these vectors of proportions for FAST (red), GFSR (green), and SVD-GP (blue) by eigenfunction in Scenario S1 (first row) and Scenario S2 (second row). FAST achieves nearly nominal coverage for all FPCs in both scenarios and outperforms both GFSR and SVD-GP.

We extended the simulations both to a larger observation grid $M = 60$ and to a multi-level scenario; see results in Supplement Sections S3.2 and S3.3, respectively. Results were qualitatively similar with those presented here. However, for multilevel we compared our approach only to GFSR, which is the only other method with a multilevel implementation.

Table 1 provides computation times (on a personal laptop) as both N (number of subjects) and M (number of grid points) scale up for scenario S1. The left side of the table provides times for fixed $N = 50$ and $M = 30, 100, 300, 1000$, while the right side of the table provides times for fixed $M = 30$ and $N = 50, 100, 300, 1000$. The SVD-GP method does not scale up with the number of observations, M . It requires more than 100 minutes for $N = 50, M = 300$ and exhausts available memory for $N = 50, M = 1000$. In contrast, the GFRS method scales well in terms of M , but does not scale up with N . For example,

GFRS required more than 100 minutes for $N = 300, M = 30$ and more than 24 hours for $N = 1000, M = 30$. FAST scales almost linearly with both N and M , which agrees with complexity analysis of the methods. Indeed, FAST is at most linear in both N and M , while SVD-GP performs $O(M^3)$ computations and GFRS performs $O(N^3)$ computations [33].

Fixed $N = 50$				Fixed $M = 30$			
Times (min)				Times (min)			
M	FAST	GFRS	SVD-GP	N	FAST	GFRS	SVD-GP
30	1.1	4.4	1.9	50	1.0	4.1	2.5
100	1.9	8.0	11.2	100	1.7	13.4	2.9
300	4.3	15.4	124.6	300	5.4	130.6	5.8
1000	18.0	64.6	—	1000	18.2	—	27.8

Table 1: Table of observed computational times for each combination of scale and method (simulation S1). SVD-GP exceeded available RAM (16GB) when $N = 50, M = 1000$, and GFRS was stopped prematurely for $N = 1000, M = 30$ due to taking longer than 2 days.

5 Data analysis

5.1 The DASH4D CGM Study

Dietary Approaches to Stop Hypertension for Diabetes (DASH4D, NCT04286555) is a nutritional trial designed to assess how blood pressure and glucose respond to combinations of DASH-style and low-sodium diets in persons with type 2 diabetes (T2D). The study team prepared four diets: DASH4D diet with lower sodium, DASH4D diet with higher sodium, Comparison diet with lower sodium, and Comparison diet with higher sodium. Weight was held constant by adjusting calorie levels, if needed. Effects of these diets were observed through a single-site, 4-period crossover design [22]. Each period consisted of 5 weeks of feeding a diet followed by at least a 1-week break (median 2 weeks). There were $N = 105$ randomized T2D participants recruited from the Baltimore area, of which $N = 65$ had meal timing data. Participants with meal timing data had median age 68 years, were 66% female, and had the following race distribution: 6.2% Asian, 87.7% Black, and 6.2% White.

Within the context of DASH4D, the DASH4D CGM study was conducted to evaluate the impact of the dietary intervention on glucose assessed by CGM. Participants wore the Abbott Freestyle Libre Pro (Abbott Diabetes Care), placed near the middle of the third week and worn into the fifth week for each feeding period. The CGM devices were placed on the back of the upper arm (approved location) by trained technicians [10]. These devices

record interstitial glucose every 15 minutes. The Libre Pro is a masked CGM system, so participants were not aware of the glucose measurements.

5.2 Mealtime CGM glucose

During feeding periods participants ate meals at the study site 3 days each week. Clinic staff observed consenting participants during these visits to document the time of meal initiation. We used these timestamps to align CGM data into 5 hour periods starting 1 hour before and ending 4 hours after meal initiation. For each participant, there were up to 20 such five-hour periods. The final dataset comprised 768 meals over 65 individuals.

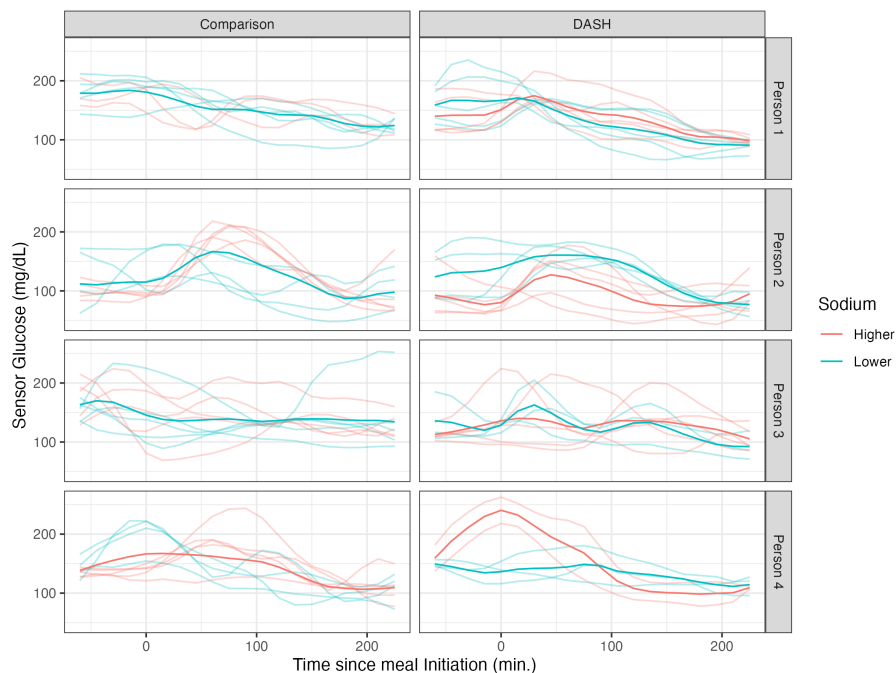


Figure 4: Mealtime CGM for 4 participants (one per row), for the DASH (left panels), Comparison (right panels) diets, lower sodium (blue curves), and higher sodium (red curves) diets. X-axis: time from meal initiation, y-axis: CGM in mg/dL. Person- and diet-specific average curves are darker, while meal-specific curves are lighter.

Figure 4 provides a visualization of mealtime CGM for four randomly-sampled study participants. The x-axis in each panel corresponds to time in minutes from meal initiation; the y-axis is the recorded interstitial glucose. Each row of two panels reports the CGM curves for one participant. The first column is for Comparison meals, and the second is for DASH meals. The curve color corresponds to lower or higher sodium diets, and the darker curves are the within-person average curves.

The data structures in Figure 4 suggest applying either Bayesian FPCA to the participant average curves or using a two-level Bayesian FPCA to capture both the participant-

specific averages (level 1) and the meal-specific deviations (level 2) within each diet. We undertake these analyses in Sections 5.3 and 5.4 respectively.

5.3 Bayesian FPCA of average CGM within diets

We fit Fast BayesFPCA to the participant average CGM curves for each diet separately (darker curves in Figure 4) and compared results across diets. We use spline basis of dimension $Q = 10$ for $K = 3$ eigenfunctions. The number of curves per-diet ranges between 36 – 49, so accounting for variability in FPC estimates is of particular importance [13].

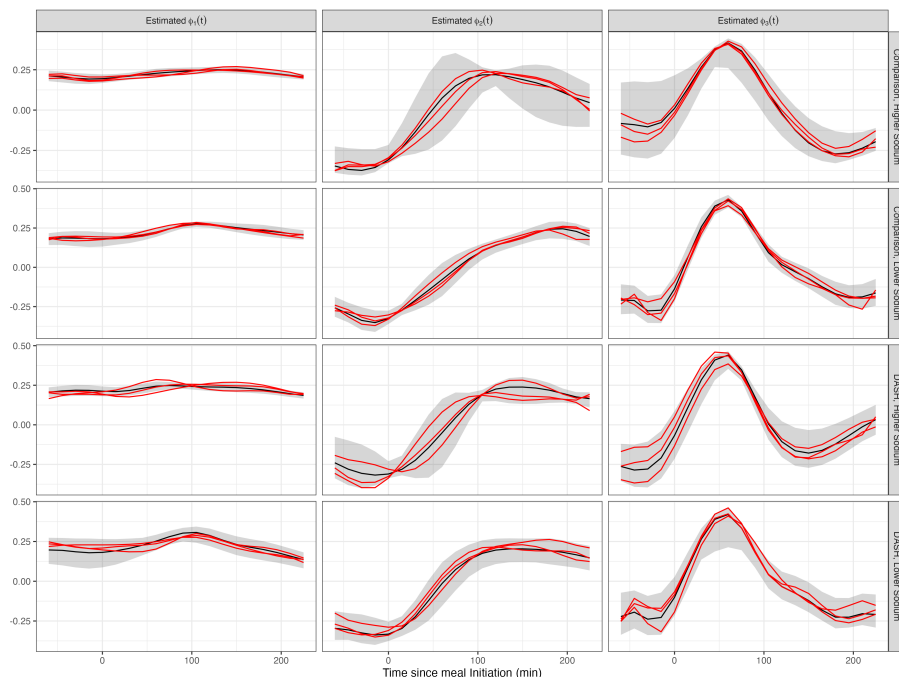


Figure 5: Bayesian FPCA results for the first three PCs (one FPC per column) for each of the four diets (on diet per row). X-axis: time from the start of the meal. Black curves: posterior mean; red curves: three samples from the posterior of the PCs; shaded areas: pointwise 95% credible intervals.

Figure 5 displays results for Bayesian FPCA inference for the first three PCs (one column each) for the four diets (one row each). For all panels the x-axis is the time from the start of the meal, the black curves are the posterior means, the red curves are three samples from the posterior of the PCs, and the shaded areas are point-wise, equal-tail 95% credible intervals. We visualize the posterior samples to better demonstrate joint sampling variability in the set of eigenfunctions. Each set of red FPC curves corresponding to the same iteration is a posterior realization on the Stiefel manifold.

Figure 6 visualizes how the mealtime glucose variability decomposes among the eigenfunctions of Figure 5. The left panel indicates the mean and equal-tail 95% credible interval

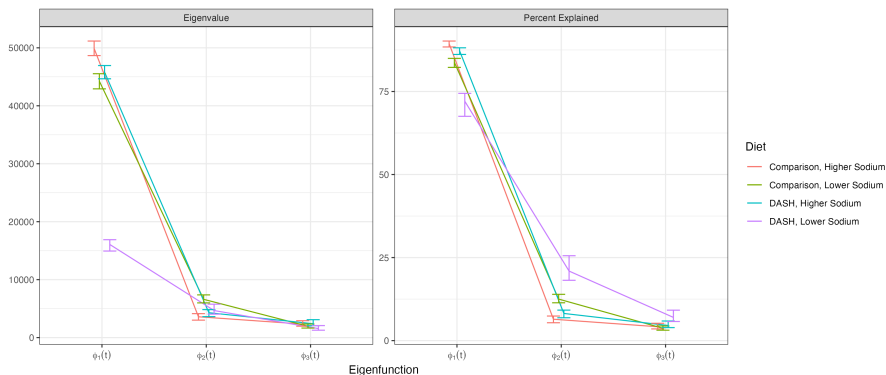


Figure 6: Eigenvalue and percent-variability estimates from the Bayesian FPCA models fit to each of the four diets (each line and color corresponds to one diet). X-axis: eigenfunction corresponding to eigenvalue/percent variance explained. All estimates are presented with their corresponding 95% credible intervals.

of eigenvalues associated with each FPC and diet, while the right provides the corresponding percent variability quantities. Each diet is shown using a distinct color.

Posterior eigenfunction estimates $\hat{\phi}_k(t)$ are qualitatively similar across diets in Figure 5. The primary modes of variability $\hat{\phi}_1(t)$ are nearly constant with a small curvature. Higher scores on these components correspond to higher CGM responses over the entire mealtime period. The sample-to-sample variability in the shape of $\phi_1(t)$ is low, indicating confidence in the posterior mean curves. As indicated by Figure 6, $\hat{\phi}_1(t)$ always explains the majority of observed variability. This reinforces existing literature on the importance of mean postprandial glucose level [12].

We consider the $\hat{\phi}_2(t)$ and $\hat{\phi}_3(t)$ together, as they explain a small proportion of the observed variability. The second FPCs, $\hat{\phi}_2(t)$, generally have an *S* pattern, such that larger scores correspond to lower glucose in the pre-prandial hour, increase over the hour post-meal, and a larger response two to four hours after eating. The third FPCs, $\hat{\phi}_3(t)$, are negative during the hour before the meal, increase quickly to a peak positive value about 50 to 70 minutes after food intake, and decrease relatively quickly back to negative values about 150–200 minutes after the meal. Higher scores on $\hat{\phi}_3(t)$ correspond to below-average glucose before the meal and rapid glucose uptake after the meal. The sample-to-sample variability of both the $\phi_2(t)$ and $\phi_3(t)$ estimators is higher than that of $\phi_1(t)$, which is likely due to the smaller signal; for further discussion, see [11].

The variability of the glucose response in the DASH/lower sodium diet is much lower than for all other three diets; note in Figure 6 that $\hat{\lambda}_1(t)$ is 3 to 4 times smaller for this diet compared with all others. This diet is of primary interest to the DASH4D study, and appears to be associated with lower inter-participant variability in mean glucose level. This finding requires validation, but could indicate a more stable glycemic response for

individuals on this diet.

Fast BayesFPCA produced reasonable results, qualitatively consistent with standard FPCA, across all four diets. Each model took just over a minute to fit on a standard laptop using 4500 warm-up samples and 500 posterior samples.

Note that the mean CGM curves are derived from differing numbers of curves for each participant, potentially causing different sampling variability. We can instead randomly select single curves from each participant (completed in Supplement Section S4 with qualitatively similar results). To both appropriately model all sources of variability within each diet and use all data, we turn to multilevel FPCA.

5.4 Bayesian MFPCA of individual CGM curves

We fit the multilevel extension of Fast BayesFPCA described in Section 2.5 for each diet separately, where meals are nested within participants. We use spline basis dimension $Q = 10$, $K_1 = 2$ eigenfunctions at the subject level, and $K_2 = 3$ eigenfunctions at the meal level. The number of observed meals ranges from 147 to 219 for each diet, with at most five meals per participant. As there is no reason to assume that meal/visit order has effect, for this analysis we set $\eta_j(t) = 0$ for all j .

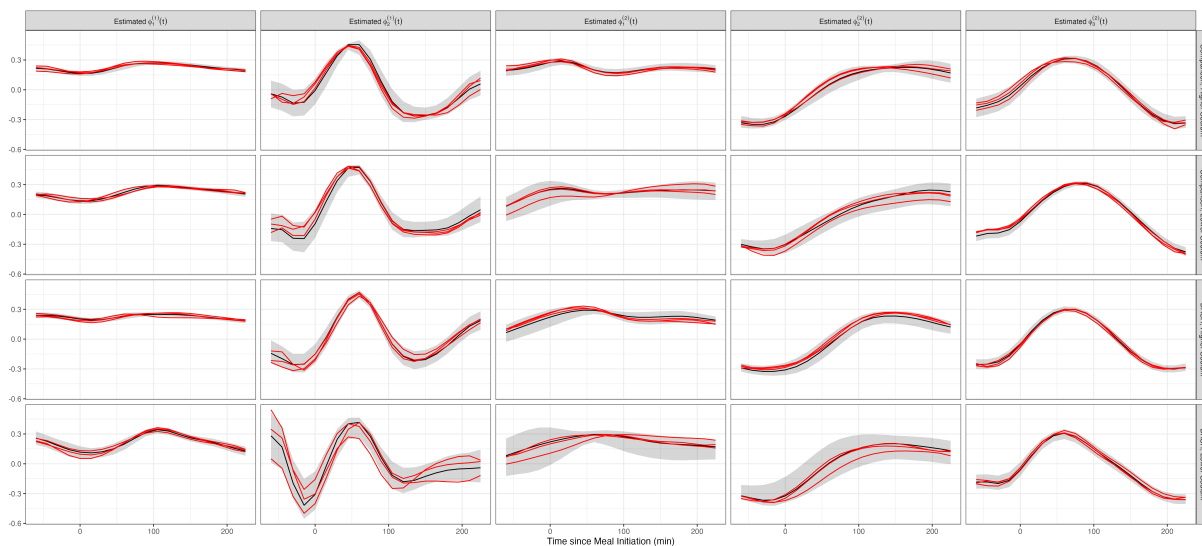


Figure 7: Bayesian MFPCA results for the first two PCs at the subject level and first three PCs at the meal level. Each column corresponds to an FPC and each row corresponds to a diet. X-axis: time from the meal start. Black curves: posterior mean; red curves: three samples from the posterior of the PCs; shaded areas: pointwise 95% credible intervals.

Figure 7 displays the Bayesian MFPCA results, with row indicating diet and column indicating FPC. The first two columns correspond to the subject level, while the last three correspond to the meal level. For each panel, the x-axis is the time from the start of the

meal, the black curves are the posterior means, the red curves are three samples from the posterior of the FPCs, and the shaded areas are pointwise, equal-tail 95% credible intervals. Each set of red FPC curves corresponding to the same iteration is a posterior realization on the subject- and meal-level Stiefel manifolds.

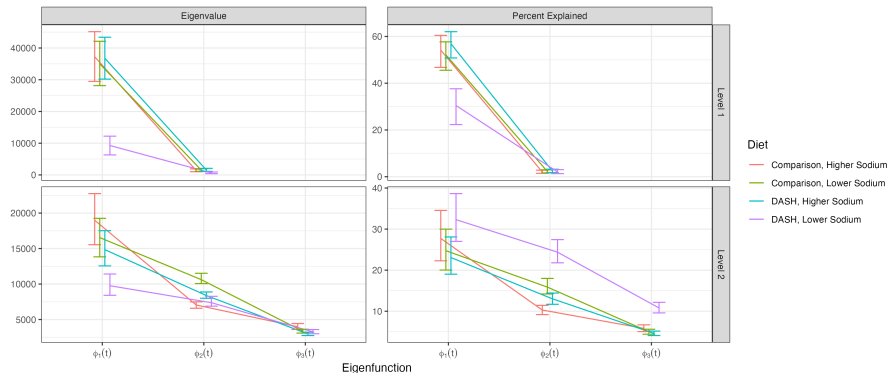


Figure 8: Eigenvalues (left panels), percent-variability explained (right panels) within level and diet, and 95% credible intervals for the Bayesian MFPCA models fit to the four diets (color corresponds to diet) at subject (first row of panels) and meal (second row of panels) levels. X-axis: eigenfunction number.

Figure 8 illustrates the estimated variability (left panels) and percent variability explained (right panels) within level and diet, as well as the 95% credible intervals. The first row of panels corresponds to the subject level (level 1) while the second row of panels corresponds to the meal level (level 2). Each color corresponds to a diet and the fast Bayes MFPCA was fit separately for each diet. As in the single level case, the DASH/lower sodium diet exhibits less variability among subject-specific glucose response (compare first row, first column in Figure 8 to the first panel in Figure 6.) This difference can be observed also in terms of meal-to-meal variability, which is lower for the DASH/lower sodium diet. Another important feature is that the second eigenvalues at the subject level are very small and much smaller than the first two eigenvalues at the meal level (compare the first row, first column and second row, first column panels in Figure 8). This suggests that most of the observed variability can be partitioned in a constant vertical shift at the subject level and some more complex meal-to-meal variability.

As in the single level analyses, Figure 7 indicates qualitative similarity of estimates $\widehat{\phi}_k^{(1)}(t), \widehat{\phi}_l^{(2)}(t)$ across diets. The primary mode of variability within each diet is $\widehat{\phi}_1^{(1)}(t)$, a nearly constant function. Higher subject scores on this component correspond to higher subject-specific glucose over the entire observation window. The sample-to-sample variability in the shape of $\phi_1^{(1)}(t)$ is consistently low, indicating confidence in this functional form. There is some heterogeneity in the percent variability explained by this component, but it is $\geq 35\%$ for every diet. The first eigenfunction at the second level, $\widehat{\phi}_1^{(2)}(t)$, is also

nearly constant with a small curvature and low sampling variability. They explain between 23 – 33% of the total variability according to Figure 8, indicating that a constant shift is the main source of variation both among individuals and within-individuals between meals. The second eigenfunction at the meal level, $\widehat{\phi}_2^{(2)}(t)$, explains 10 – 25% of the total variability and has an *S* pattern. As in the single-level case, larger scores on $\widehat{\phi}_2^{(2)}(t)$ correspond to lower pre-prandial glucose, increase over the hour post-meal, and a larger response two to four hours after the meal. The eigenfunctions $\widehat{\phi}_2^{(1)}(t)$, $\widehat{\phi}_3^{(2)}(t)$ capture higher-order glycemic reaction patterns and explain much smaller proportions of variability (< 12%).

Each Bayesian MFPCA model takes ≈ 15 minutes to run on a standard laptop with 4500 warm-up samples and 500 samples from the posterior. We use this large number of warm-up samples out of an abundance of caution. Simulations indicate that as little as 1000 warm-up samples could be used.

5.5 Model Checking

Model diagnostics were conducted to study MCMC convergence. We generate trace plots of eigenfunctions evaluated at $t = -45, 75$, and 210 minutes relative to meal initialization. These trace plots, found in Supplement Sections S5 and S6, display posterior samples from 4 chains in different colors. For all eigenfunctions from both FPCA and MFPCA, the trace plots demonstrate good mixing and minimal autocorrelation.

To investigate whether our FPCA and MFPCA models fit the data well, we compared posterior samples of underlying smooths to the raw data. These smooths are calculated as $\widehat{Y}_i(t) = \widehat{\mu}(t) + \sum_{k=1}^K \widehat{\xi}_{ik} \widehat{\phi}_k(t)$ for FPCA and $\widehat{Y}_{ij}(t) = \widehat{\mu}(t) + \sum_{k=1}^{K_1} \widehat{\xi}_{ik} \widehat{\phi}_k^{(1)}(t) + \sum_{l=1}^{K_2} \widehat{\zeta}_{ijl} \widehat{\phi}_l^{(2)}(t)$ for MFPCA. We compare 100 samples of these smooths (black curves) to the observed data (red curves) for the same four participants shown in Figure 4; see Supplemental Figures S13 and S17. The posterior samples of the smooth estimators provide reasonable approximations of the observed data.

6 Discussion

FPCA is one of the most popular statistical methods relying on the estimated eigenfunctions or FPCs of the covariance operator of a data matrix. Standard implementations of FPCA estimate the FPCs and then treat them as fixed in subsequent analysis, potentially understating the observed variability and impacting downstream inference. In this paper we propose Fast BayesFPCA, a Bayesian method treating the FPCs as parameters on the corresponding Stiefel manifold and using MCMC simulation to explore their joint posterior.

The main idea of the approach is to represent the FPCs using an orthonormal spline basis, inducing a uniform prior on the linear subspace of smooth functions within the high dimensional Stiefel manifold that supports the eigenfunctions in the data space. This

approach directly samples all model components, and avoids computational bottleneck due to the high dimensional Stiefel manifold.

Through visualization of the model component samples, Fast BayesFPCA provides intuition for how the model posterior surface maps to the high-dimensional Stiefel manifold geometry. These visualizations are useful for identifying potential problems, such as weak identifiability or multi-modality of the posterior distribution. Any Bayesian implementation of FPCA could, in theory, be used for this purpose. However, Fast BayesFPCA proved to be easy to use for this purpose because of its simplified parameter space.

Many open questions remain, including: (1) the generalizability and feasibility of these ideas for non-Gaussian outcomes; (2) theoretical guarantees and non-uniform priors on the Stiefel manifolds; (3) how methods can be further computationally improved.

References

- [1] Barua, S., R. A Wierchowska-McNew, N. E. P. Deutz, and A. Sabharwal (2022, October). Discordance between postprandial plasma glucose measurement and continuous glucose monitoring. *The American Journal of Clinical Nutrition* 116(4), 1059–1069.
- [2] Brumback, B., D. Ruppert, and M. Wand (1999). Comment on variable selection and function estimation in additive nonparametric regression using data-based prior by Shively, Kohn, and Wood. *Journal of the American Statistical Association* 94(447), 794–797.
- [3] Carpenter, B., A. Gelman, M. D. Hoffman, D. Lee, B. Goodrich, M. Betancourt, M. Brubaker, J. Guo, P. Li, and A. Riddell (2017, January). Stan: A Probabilistic Programming Language. *Journal of Statistical Software* 76, 1–32.
- [4] Chikuse, Y. (2003). *Statistics on Special Manifolds*, Volume 174 of *Lecture Notes in Statistics*. New York, NY: Springer. Edited by Bickel, P. and Diggle, P. and Fienberg, S. and Krickeberg, K. and Olkin, I. and Wermuth, N. and Zeger, S.
- [5] Crainiceanu, C., D. Ruppert, and M. Wand (2005). Bayesian analysis for penalized spline regression using winbugs. *Journal of Statistical Software* 14(14), 1–24.
- [6] Crainiceanu, C. M. and A. J. Goldsmith (2010, January). Bayesian Functional Data Analysis Using WinBUGS. *Journal of Statistical Software* 32, 1–33.
- [7] Crainiceanu, C. M., J. Goldsmith, A. Leroux, and E. Cui (2024). *Functional Data Analysis with R*. Springer New York, NY, USA.
- [8] Craven, P. and G. Wahba (1979). Smoothing noisy data with spline functions. *Numerische Mathematik* 1, 377–403.
- [9] Di, C.-Z., C. M. Crainiceanu, B. S. Caffo, and N. M. Punjabi (2009, March). Multilevel functional principal component analysis. *The Annals of Applied Statistics* 3(1), 458–488. Publisher: Institute of Mathematical Statistics.
- [10] FDA Report on Freestyle Libre Pro (2016, September). Abbott Freestyle Libre Pro Summary of Safety and Effectiveness Data. https://www.accessdata.fda.gov/cdrh_docs/pdf15/p150021b.pdf.
- [11] Fisher, A., B. Caffo, B. Schwartz, and V. Zipunnikov (2014, 05). Fast, exact bootstrap principal component analysis for $p > 1$ million. *Journal of the American Statistical Association* 111(514), 846–860.

- [12] Garber, A. J. (2012, October). Postprandial Dysmetabolism and the Heart. *Heart Failure Clinics* 8(4), 563–573.
- [13] Goldsmith, J., S. Greven, and C. Crainiceanu (2013). Corrected confidence bands for functional data using principal components. *Biometrics* 69(1), 41–51.
- [14] Goldsmith, J., V. Zipunnikov, and J. Schrack (2015, June). Generalized Multilevel Function-on-Scalar Regression and Principal Component Analysis. *Biometrics* 71(2), 344–353.
- [15] Greven, S., C. Crainiceanu, B. Caffo, and D. Reich (2010). Longitudinal functional principal component analysis. *Electronic journal of statistics* 4, 1022–1054.
- [16] Hershon, K. S., B. R. Hirsch, and O. Odugbesan (2019, July). Importance of Postprandial Glucose in Relation to A1C and Cardiovascular Disease. *Clinical Diabetes : A Publication of the American Diabetes Association* 37(3), 250–259.
- [17] James, I. (1976). *The Topology of Stiefel Manifolds*. Cambridge University Press.
- [18] Jauch, M., P. D. Hoff, and D. B. Dunson (2021, September). Monte Carlo Simulation on the Stiefel Manifold via Polar Expansion. *Journal of Computational and Graphical Statistics* 30(3), 622–631. Publisher: Taylor & Francis eprint: <https://doi.org/10.1080/10618600.2020.1859382>.
- [19] Kai-Tai Fang and Run-Ze Li (1997, March). Some methods for generating both an NT-net and the uniform distribution on a Stiefel manifold and their applications. *Computational Statistics & Data Analysis* 24(1), 29–46.
- [20] Kimeldorf, G. and G. Wahba (1970). A correspondence between bayesian estimation on stochastic processes and smoothing by splines. *The Annals of Mathematical Statistics* 41(2), 495–502.
- [21] Mardia, K. and C. Khatri (1977). Uniform distribution on a stiefel manifold. *Journal of Multivariate Analysis* 7(3), 468–473.
- [22] NIH Reporting DASH4D (2024). Project details: Effects of the dash diet on glucose patterns in adults with type 2 diabetes. https://reporter.nih.gov/search/W2pb_quLtk0En58czHh1wA/project-details/10829865.
- [23] Nolan, T. H., S. Richardson, and H. Ruffieux (2025, March). Efficient Bayesian functional principal component analysis of irregularly-observed multivariate curves. *Computational Statistics & Data Analysis* 203, 108094.

- [24] O’Sullivan, F. (1986). A statistical perspective on ill-posed inverse problems (with discussion). *Statistical Science* 1(4), 505–527.
- [25] Peng, J. and D. Paul (2009, January). A Geometric Approach to Maximum Likelihood Estimation of the Functional Principal Components From Sparse Longitudinal Data. *Journal of Computational and Graphical Statistics* 18(4), 995–1015. Publisher: ASA Website _eprint: <https://doi.org/10.1198/jcgs.2009.08011>.
- [26] Ruppert, D., M. Wand, and R. Carroll (2003). *Semiparametric Regression*. Cambridge Series in Statistical and Probabilistic Mathematics. Cambridge University Press.
- [27] Röhling, M., T. Martin, M. Wonnemann, M. Kragl, H. H. Klein, L. Heinemann, S. Martin, and K. Kempf (2019, September). Determination of Postprandial Glycemic Responses by Continuous Glucose Monitoring in a Real-World Setting. *Nutrients* 11(10), 2305.
- [28] Shepard, R., S. R. Brozell, and G. Gidofalvi (2015, July). The Representation and Parametrization of Orthogonal Matrices. *The Journal of Physical Chemistry A* 119(28), 7924–7939. Publisher: American Chemical Society.
- [29] Shou, H., V. Zipunnikov, C. Crainiceanu, and S. Greven (2015). Structured functional principal component analysis. *Biometrics* 71(1), 247–257.
- [30] Wahba, G. (1983). Bayesian “Confidence Intervals” for the Cross-Validated Smoothing Spline. *Journal of the Royal Statistical Society: Series B* 45(1), 133–150.
- [31] Weisstein, E. W. (2002). Legendre Polynomial. Publisher: Wolfram Research, Inc.
- [32] Wood, S. (2006). *Generalized Additive Models: An Introduction with R*. Chapman and Hall/CRC.
- [33] Wood, S. N. (2000, July). Modelling and Smoothing Parameter Estimation With Multiple Quadratic Penalties. *Journal of the Royal Statistical Society Series B: Statistical Methodology* 62(2), 413–428.
- [34] Ye, J. (2024, May). Functional principal component models for sparse and irregularly spaced data by Bayesian inference. *Journal of Applied Statistics* 51(7), 1287–1317. Publisher: Taylor & Francis _eprint: <https://doi.org/10.1080/02664763.2023.2197587>.
- [35] Zipunnikov, V., B. Caffo, D. Yousem, C. Davatzikos, B. Schwartz, and C. Crainiceanu (2011). Multilevel functional principal component analysis for high-dimensional data. *Journal of Computational and Graphical Statistics* 20(4), 852–873.

SUPPLEMENTARY MATERIAL

S1 Penalty matrix \mathbf{P}_α

Recall we chose a penalty with form $\alpha \int f^2(t)dt + (1 - \alpha) \int \{f''(t)\}^2 dt$. There exist unique and specific penalty matrices $\mathbf{P}_0, \mathbf{P}_2$ such that $\int f^2(t)dt \approx \theta^t \mathbf{P}_0 \theta$ and $\int \{f''(t)\}^2 dt \approx \theta^t \mathbf{P}_2 \theta$ [8, 20, 24, 30]. We follow [14] and define $\mathbf{P}_\alpha = \alpha \mathbf{P}_0 + (1 - \alpha) \mathbf{P}_2$. Using this notation, we find that $\alpha \int f^2(t)dt + (1 - \alpha) \int \{f''(t)\}^2 dt \approx \theta^t \mathbf{P}_\alpha \theta$.

We proceed by defining both of the penalty components $\mathbf{P}_0, \mathbf{P}_2$ separately, as the final penalty \mathbf{P}_α is just a linear combination of these matrices. Let $\mathbf{B}(t) = [b_1(t) | \dots | b_Q(t)]$ represent the orthonormal basis functions, such that $\mathbf{B} = \mathbf{B}(T) = [b_1(T) | \dots | b_Q(T)] \in \mathbb{R}^{M \times Q}$. First, for the zero-order penalty, \mathbf{P}_0 :

$$\mathbf{P}_0 = \frac{1}{M} \mathbf{B}^t \mathbf{B}$$

Next, the "wiggleness" penalty \mathbf{P}_2 . For this penalty, based on the squared second derivative, we introduce the second derivative matrix $\mathbf{B}'' = \mathbf{B}''(T) = [b_1''(T) | \dots | b_Q''(T)] \in \mathbb{R}^{M \times Q}$. We evaluate this matrix using the known derivatives for spline functions, but it can also be approximated numerically.

$$\mathbf{P}_2 = \frac{1}{M} (\mathbf{B}'')^t (\mathbf{B}'')$$

Combining these two penalties, we can define the linear combination \mathbf{P}_α , which will be non-degenerate when $\alpha > 0$.

$$\begin{aligned} \mathbf{P}_\alpha &= \alpha \mathbf{P}_0 + (1 - \alpha) \mathbf{P}_2 \\ &= \frac{1}{M} [\alpha \mathbf{B}^t \mathbf{B} + (1 - \alpha) (\mathbf{B}'')^t (\mathbf{B}'')] \end{aligned}$$

S2 Full conditional posteriors

As the eigenfunction and score posteriors are presented in the main text, we focus instead on the fixed effects spline coefficients w_μ , the eigenvalues λ_k , the smoothing parameters h_μ, h_k $k \in \{1, \dots, K\}$, and the noise variance σ^2 . First, for the fixed effects weights w_μ :

$$\begin{aligned}
[w_\mu | \text{others}] &\propto \prod_{i=1}^N \prod_{m=1}^M N\{Y_i(t_m) | (\mathbf{B}w_\mu)_m + \sum_{k=1}^K \xi_{ik} (\mathbf{B}\psi_k)_m, \sigma^2\} \times \exp\left(-\frac{h_\mu}{2\sigma^2} w_\mu^t \mathbf{P}_\alpha w_\mu\right) \\
&\propto \exp\left\{-\frac{1}{2\sigma^2} \sum_{i=1}^N [\mathbf{B}w_\mu - (Y_i(T) - \sum_{k=1}^K \xi_{ik} \mathbf{B}\psi_k)]^t [\mathbf{B}w_\mu - (Y_i(T) - \sum_{k=1}^K \xi_{ik} \mathbf{B}\psi_k)] - \frac{h_\mu}{2\sigma^2} w_\mu^t \mathbf{P}_\alpha w_\mu\right\} \\
&\propto \exp\left\{-\frac{1}{2\sigma^2} \sum_{i=1}^N [w_\mu^t \mathbf{B}^t \mathbf{B} w_\mu - 2(Y_i(T) - \sum_{k=1}^K \xi_{ik} \mathbf{B}\psi_k)^t \mathbf{B} w_\mu] - \frac{h_\mu}{2\sigma^2} w_\mu^t \mathbf{P}_\alpha w_\mu\right\} \\
&\propto \exp\left\{-\frac{1}{2\sigma^2} [N w_\mu^t w_\mu - 2 \sum_{i=1}^N (Y_i(T)^t \mathbf{B} w_\mu - \sum_{k=1}^K \xi_{ik} \psi_k^t \mathbf{B}^t \mathbf{B} w_\mu)] - \frac{h_\mu}{2\sigma^2} w_\mu^t \mathbf{P}_\alpha w_\mu\right\} \\
&\propto \exp\left\{-\frac{1}{2} [w_\mu^t (\frac{N \mathbf{I}_Q + h_\mu \mathbf{P}_\alpha}{\sigma^2}) w_\mu - \frac{2}{\sigma^2} \sum_{i=1}^N (Y_i(T)^t \mathbf{B} - \sum_{k=1}^K \xi_{ik} \psi_k^t) w_\mu]\right\}
\end{aligned}$$

In the above, we recognize the form of a multivariate normal distribution. The explicit parameterization is as follows:

$$[w_\mu | \text{others}] \sim MVN((N \mathbf{I}_Q + h_\mu \mathbf{P}_\alpha)^{-1} \sum_{i=1}^N [\mathbf{B}^t Y_i(T) - \sum_{k=1}^K \xi_{ik} \psi_k], \sigma^2 (N \mathbf{I}_Q + h_\mu \mathbf{P}_\alpha)^{-1})$$

While this posterior distribution is not necessarily trivial to derive, the resulting multivariate normal is relatively simple to sample given the other parameters and data.

Moving onto the eigenvalues λ_k , where IG represents the inverse gamma distribution:

$$\begin{aligned}
[\lambda_k | \text{others}] &\propto \prod_{i=1}^N N(\xi_{ik} | 0, \lambda_k) \text{IG}(\lambda_k | \alpha_\lambda, \beta_\lambda) \\
&\propto \prod_{i=1}^N \left\{ \lambda_k^{-\frac{1}{2}} \exp\left(-\frac{\xi_{ik}^2}{2\lambda_k}\right) \right\} \times \lambda_k^{-\alpha_\lambda - 1} \exp\left(-\frac{\beta_\lambda}{\lambda_k}\right) \\
&\propto \lambda_k^{-(\frac{N}{2} + \alpha_\lambda) - 1} \exp\left(-\left(\frac{1}{2} \sum_{i=1}^N \xi_{ik}^2 + \beta_\lambda\right) \times \frac{1}{\lambda_k}\right)
\end{aligned}$$

As was intended when choosing the conjugate prior, the above density has the form of the inverse-gamma. The exact parameterization is as follows:

$$[\lambda_k | \text{others}] \sim \text{IG}\left(\frac{N}{2} + \alpha_\lambda, \frac{1}{2} \sum_{i=1}^N \xi_{ik}^2 + \beta_\lambda\right)$$

Consider next the smoothing parameters h_μ, h_k for $k \in \{1, 2, \dots, K\}$. We derive the posterior for h_μ first:

$$\begin{aligned} [h_\mu | \text{others}] &\propto \exp\left(-\frac{h_\mu}{2\sigma^2} w_\mu^t \mathbf{P}_\alpha w_\mu\right) \times \Gamma(\alpha_\mu, \beta_\mu) \\ &\propto \exp\left(-\frac{h_\mu}{2\sigma^2} w_\mu^t \mathbf{P}_\alpha w_\mu\right) \times h_\mu^{\alpha_\mu - 1} \exp(-\beta_\mu h_\mu) \\ &\propto h_\mu^{\alpha_\mu - 1} \exp\left(-\left(\frac{w_\mu^t \mathbf{P}_\alpha w_\mu}{2\sigma^2} + \beta_\mu\right) h_\mu\right) \end{aligned}$$

One can recognize the form of the gamma distribution in the last line above, leading to the conditional posterior $[h_\mu | \text{others}] \sim \Gamma(\alpha_\mu, \frac{w_\mu^t \mathbf{P}_\alpha w_\mu}{2\sigma^2} + \beta_\mu)$. We can similarly derive the conditional posterior for the general eigenfunction smoothing parameter h_k :

$$\begin{aligned} [h_k | \text{others}] &\propto \exp\left(-\frac{h_k}{2\sigma^2} \psi_k^t \mathbf{P}_\alpha \psi_k\right) \times \Gamma(\alpha_\psi, \beta_\psi) \\ &\propto \exp\left(-\frac{h_k}{2\sigma^2} \psi_k^t \mathbf{P}_\alpha \psi_k\right) \times h_k^{\alpha_\psi - 1} \exp(-\beta_\psi h_k) \\ &\propto h_k^{\alpha_\psi - 1} \exp\left(-\left(\frac{\psi_k^t \mathbf{P}_\alpha \psi_k}{2\sigma^2} + \beta_\psi\right) h_k\right) \end{aligned}$$

Once more, the form of the gamma distribution is clear in the final line above, leading to the conditional posterior $[h_k | \text{others}] \sim \Gamma(\alpha_\psi, \frac{\psi_k^t \mathbf{P}_\alpha \psi_k}{2\sigma^2} + \beta_\psi)$.

We move on finally to the conditional posterior of the noise variance σ^2 :

$$\begin{aligned} [\sigma^2 | \text{others}] &\propto \prod_{i=1}^N \prod_{m=1}^M N(Y_i(t_m) | (\mathbf{B}w_\mu)_m + \sum_{k'=1}^K \xi_{ik'} (\mathbf{B}\psi_{k'})_m, \sigma^2) \times \\ &\quad \exp\left(-\frac{h_\mu}{2\sigma^2} w_\mu^t \mathbf{P}_\alpha w_\mu\right) \times \exp\left(-\frac{1}{2\sigma^2} \sum_{k=1}^K h_k \psi_k^t \mathbf{P}_\alpha \psi_k\right) \times \text{IG}(\sigma^2 | \alpha_\sigma, \beta_\sigma) \\ &\propto \prod_{i=1}^N \prod_{m=1}^M (\sigma^2)^{-\frac{1}{2}} \exp\left(-\frac{\{Y_i(t_m) - [(\mathbf{B}w_\mu)_m + \sum_{k'=1}^K \xi_{ik'} (\mathbf{B}\psi_{k'})_m]\}^2}{2\sigma^2}\right) \times \\ &\quad \exp\left(-\frac{h_\mu}{2\sigma^2} w_\mu^t \mathbf{P}_\alpha w_\mu\right) \times \exp\left(-\frac{1}{2\sigma^2} \sum_{k=1}^K h_k \psi_k^t \mathbf{P}_\alpha \psi_k\right) \times (\sigma^2)^{-\alpha_\sigma - 1} \exp\left(-\frac{\beta_\sigma}{\sigma^2}\right) \end{aligned}$$

For the sake of simplicity and brevity, we define the residual quantity $Q_{im} = Y_i(t_m) - \{(\mathbf{B}w_\mu)_m + \sum_{k'=1}^K \xi_{ik'} (\mathbf{B}\psi_{k'})_m\}$. Proceeding from here:

$$\begin{aligned}
[\sigma^2|\text{others}] &\propto (\sigma^2)^{-\left(\frac{NM}{2}+\alpha_\sigma\right)-1} \exp\left(-\frac{\sum_{i=1}^N \sum_{m=1}^M Q_{im}^2}{2\sigma^2}\right) \times \exp\left(-\frac{h_\mu w_\mu^t \mathbf{P}_\alpha w_\mu}{2\sigma^2}\right) \times \\
&\exp\left(-\frac{1}{2\sigma^2} \sum_{k=1}^K h_k \psi_k^t \mathbf{P}_\alpha \psi_k\right) \times \exp\left(-\frac{\beta_\sigma}{\sigma^2}\right) \\
&\propto (\sigma^2)^{-\left(\frac{NM}{2}+\alpha_\sigma\right)-1} \exp\left(-\frac{1}{2\sigma^2} \left[\sum_{i=1}^N \sum_{m=1}^M Q_{im}^2 + h_\mu w_\mu^t \mathbf{P}_\alpha w_\mu + \sum_{k=1}^K h_k \psi_k^t \mathbf{P}_\alpha \psi_k + 2\beta_\sigma \right]\right)
\end{aligned}$$

The last line above is clearly the form of the inverse gamma distribution, with exact parameterization as follows:

$$[\sigma^2|\text{others}] \sim \text{IG}\left(\frac{NM}{2} + \alpha_\sigma, \frac{1}{2} \left[\sum_{i=1}^N \sum_{m=1}^M Q_{im}^2 + h_\mu w_\mu^t \mathbf{P}_\alpha w_\mu + \sum_{k=1}^K \psi_k^t \mathbf{P}_\alpha \psi_k + 2\beta_\sigma \right]\right)$$

S3 Simulations

S3.1 General information

All code used for data simulation and subsequent model fitting can be found at this GitHub repository. We compare the simulation bases with those extracted from the real data in Figure S1.

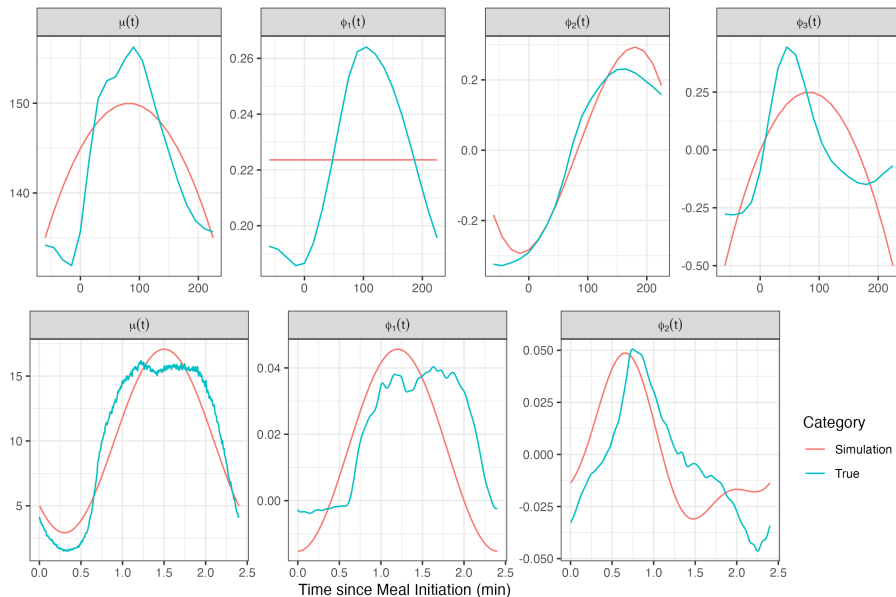


Figure S1: Comparison between functional forms used in simulations (red) and the estimates from fitting FPCA to the actual data (blue) for the two simulation scenarios. The first row corresponds to the CGM scenario, based upon the by-participant mean post-prandial CGM curves from the DASH4D study. The second row corresponds to the physical activity (PA) scenario, based upon mean MIMS data from the 2014 wave of NHANES accelerometry data.

S3.2 $M = 60$ Extension

When sampling along the functional domain more frequently ($M = 60$ rather than $M = 30$), simulation results remain qualitatively the same. Figure S2 indicates that FAST is largely non-inferior to GFSR and SVD-GP with regards to accuracy of posterior estimates of the functional components.

Figure S3 indicates that FAST achieves nominal posterior coverage of the functional components, which is not the case for GFSR nor SVD-GP.

This contrast in coverage extends to the scores, as can be observed in Figure S4.

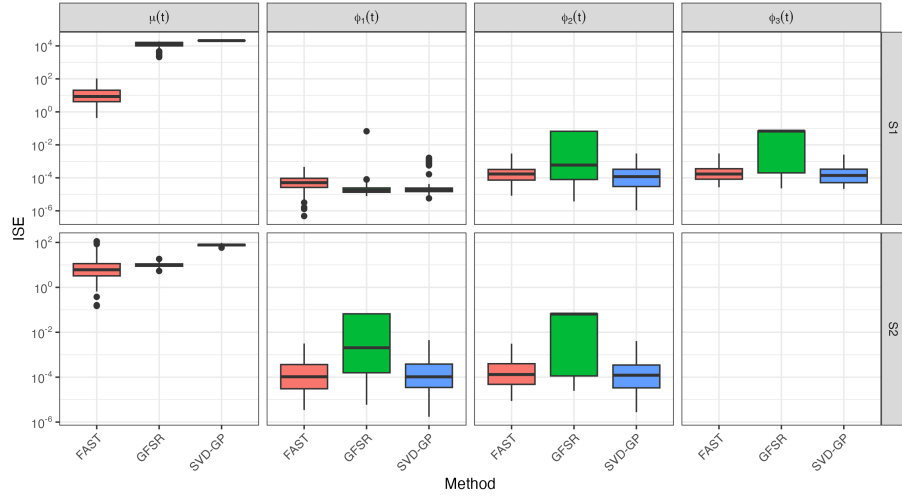


Figure S2: Boxplots of the ISE for the mean and eigenfunctions for FAST (red), GFSR (green), and SVD-GP (blue). First row: S1; second row: S2. Each column: mean or corresponding eigenfunction. Y-axis is on the log scale for presentation purposes. Results shown for $N = 50$ functions with $M = 60$ observations per function.

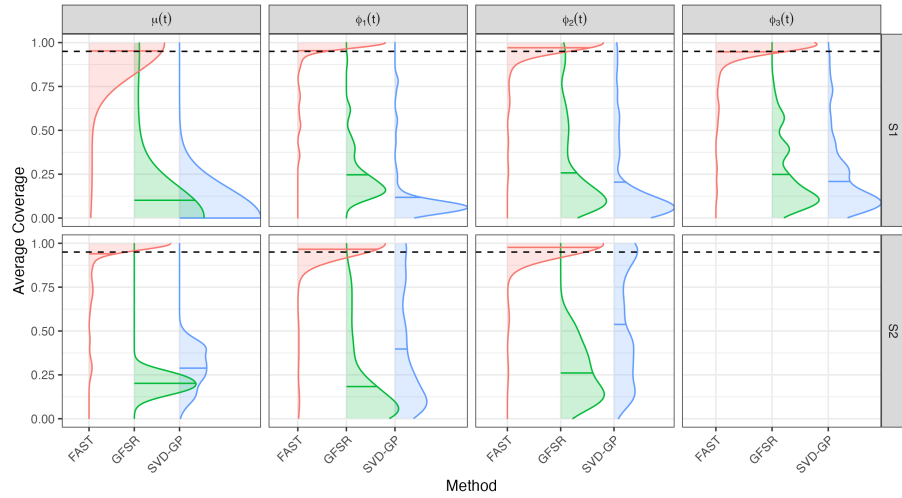


Figure S3: Kernel smoother of coverage probabilities of 95% credible intervals of the true mean and eigenfunctions for FAST (red), GFSR (green), and SVD-GP (blue). First row: S1; second row: S2. Each column: corresponding function. Distribution means: horizontal solid lines; nominal 95% level: horizontal dotted lines. Results shown for $N = 50$ functions with $M = 60$ observations per function.

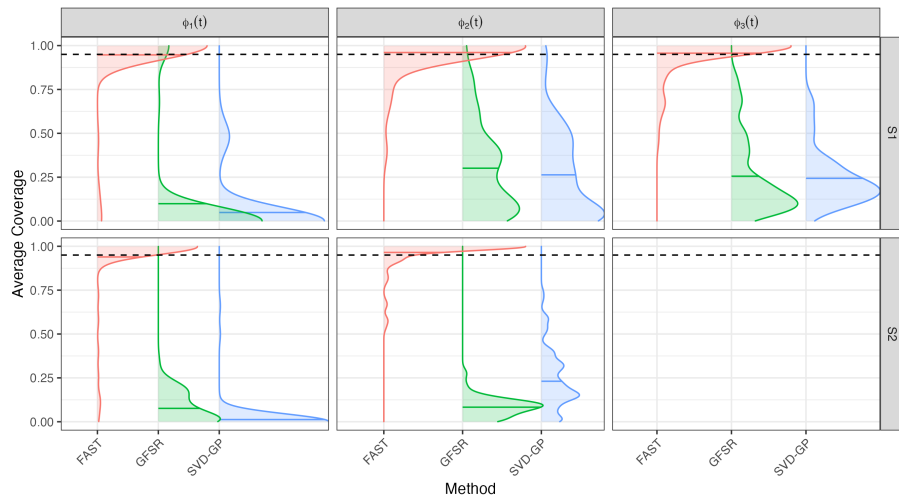


Figure S4: Kernel smoother of coverage probabilities of 95% credible intervals of the true scores, ξ_{ik}^b , for FAST (red), GFSR (green), and SVD-GP (blue). First row: S1; second row: S2. Each column: corresponding eigenfunction. Distribution means: horizontal solid lines; nominal 95% level: horizontal dotted lines. Results shown for $N = 50$ functions with $M = 60$ observations per function.

S3.3 Multilevel extension

We performed a simple 2-level simulation study to assess performance of the multilevel extension of FAST. This simulation includes 50 groups at the first level ($N = 50$), each with 5 functional observations ($\forall i, J_i = 5$) for a total of 250 functions. We were only able to compare against the GFSR approach for this simulation, as SVD-GP has no available multilevel extension. We based our study around the Fourier basis, a commonly known set of orthogonal functional bases on $t \in [0, 1]$. Here again, we apply appropriate scaling to ensure that the discretely-observed functions remain orthonormal, and we let $f_k(\cdot)$ represent Legendre polynomial of order k rescaled to $[0, 1]$ [31].

Multilevel Scenario

$$\begin{aligned} \phi_k^{(1)}(t) &= \left\{ \sqrt{\frac{2}{M}} \sin(2\pi t), \sqrt{\frac{2}{M}} \cos(2\pi t) \right\}; & \lambda_k^{(1)} &= \{10000, 2000\} \\ \phi_l^{(2)}(t) &= \left\{ \sqrt{\frac{2}{M}} \sin(4\pi t), \sqrt{\frac{2}{M}} \cos(4\pi t) \right\}; & \lambda_l^{(2)} &= \{8000, 4000\} \\ \mu(t) &= 5f_1(t) - 3f_2(t); & \sigma^2 &= 16 \end{aligned}$$

We first present the integrated squared error (ISE) of the functional components $\mu(t)$, $\phi_k^{(1)}(t)$, $\phi_l^{(2)}(t)$ in Figure S5. We calculate this measure using the same procedure detailed in Section 4. Each panel corresponds to one of the functional components, ordered from the population mean to the second level eigenfunctions. We place these plots on the log scale for presentation, as the fixed effects and eigenfunction errors are at different scales.

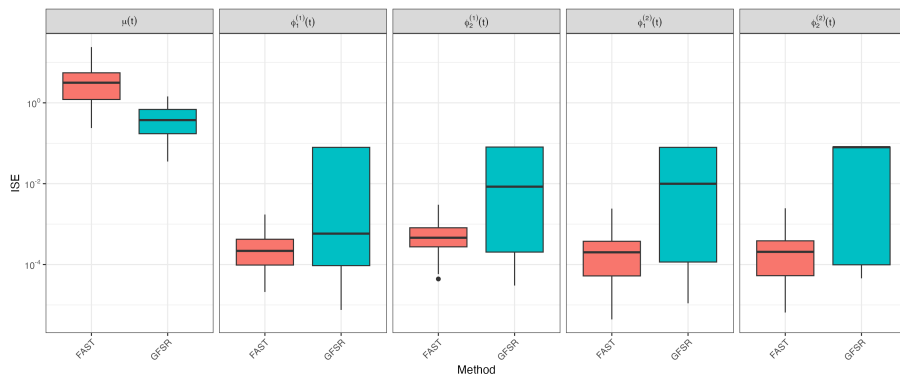


Figure S5: Boxplots of the ISE for the mean and eigenfunctions for FAST (red) and GFSR (blue) from the multilevel simulations. Y-axis is on the log scale for presentation purposes.

Figure S5 seems to indicate that GFSR has lower ISE for the fixed effects mean $\mu(t)$, but often produces much poorer posterior estimates of the eigenfunctions at both levels.

We next consider the coverage of these functional components by the point-wise equal-tailed 95% credible intervals produced by FAST and GFSR. As in Section 4, we estimate coverage probability using the proportion of time points which are covered for each simulated dataset, visualizing the result with a kernel smooth in Figure S6. We include on

this Figure the mean of each coverage distribution (horizontal solid lines) and the nominal coverage 95% coverage level (horizontal dotted lines).

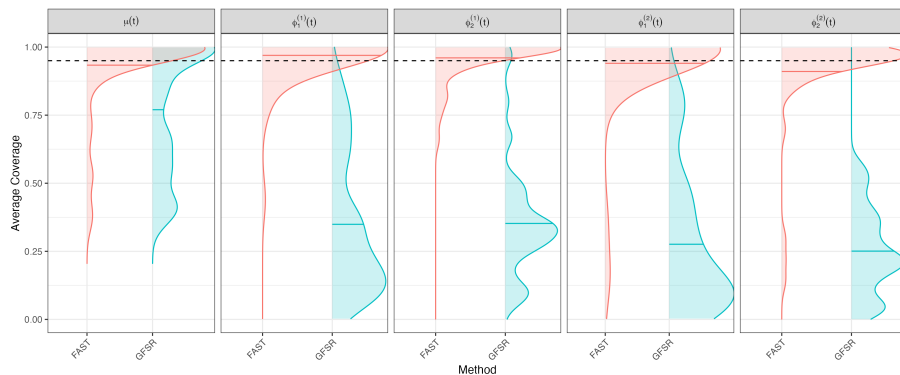


Figure S6: Kernel smoother of coverage probabilities of 95% credible intervals of the true mean and eigenfunctions for FAST (red) and GFSR (blue) from the multilevel simulations. Each column: corresponding function. Distribution means: horizontal solid lines; nominal 95% level: horizontal dotted lines.

Similar to the single-level simulations, we find that only FAST produces nearly nominal coverage of the true underlying functional components. The GFSR mean coverages range from ≈ 0.27 to ≈ 0.76 .

This disparity in coverage extends to the scores at both levels, ξ_{ik} and ζ_{ijk} , as can be observed in Figure S7. We estimate score coverage in the same fashion illustrated in Section 4. For each simulated dataset $b \leq B$, we calculate the 95% credible intervals for each individual $\xi_{ik}^b, \zeta_{ijk}^b$ from the posterior samples. We then estimate the coverage probability by aggregating the coverage indicators by the corresponding eigenfunction. Figure S7 visualizes the kernel smooths of the corresponding vectors of coverage, complete with distribution mean (solid horizontal lines) and nominal level (dashed horizontal lines). As was the case for the functional components presented in Figure S6, nominal coverage of the scores is uniquely achieved by FAST. GFSR, on the other hand, achieves mean coverages between ≈ 0.15 and ≈ 0.6 .

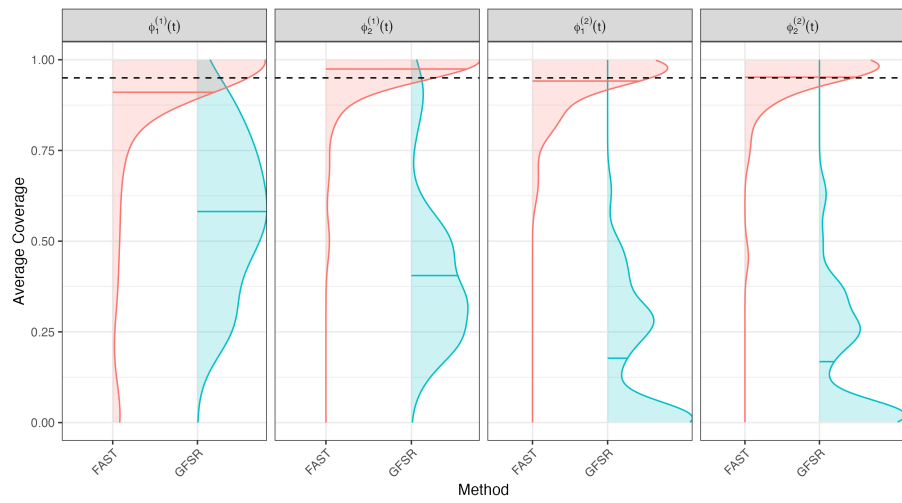


Figure S7: Kernel smoother of coverage probabilities of 95% credible intervals of the true scores, $\xi_{ik}^b, \zeta_{ijk}^b$, for FAST (red) and GFSR (blue) from the multilevel simulations. Each column: corresponding eigenfunction. Distribution means: horizontal solid lines; nominal 95% level: horizontal dotted lines.

S4 Bayesian FPCA of randomly-chosen CGM within diets

As an alternative single-level analysis, we randomly sample a function for each participant within each diet rather than aggregating. These functions each represent a single instantiation of the meal process for that participant within the particular diet, whereas the aggregate functions analyzed in Section 5.3 have varying levels of noise based upon the number of curves included in the average. However, when performing the by-diet FPCA analyses on these randomly chosen curves instead of the aggregated CGM, we observe qualitatively identical results. We first present the eigenfunctions with associated uncertainty in Figure S8. The primary difference we observe is in the additional sampling variability of $\hat{\phi}_1(t)$ for the DASH, Lower Sodium diet, along with some of the posterior samples having greater curvature. This is indicative of differences in mean mealtime glucose being much lower for this population, reduced to be on similar scale to differences peakedness.

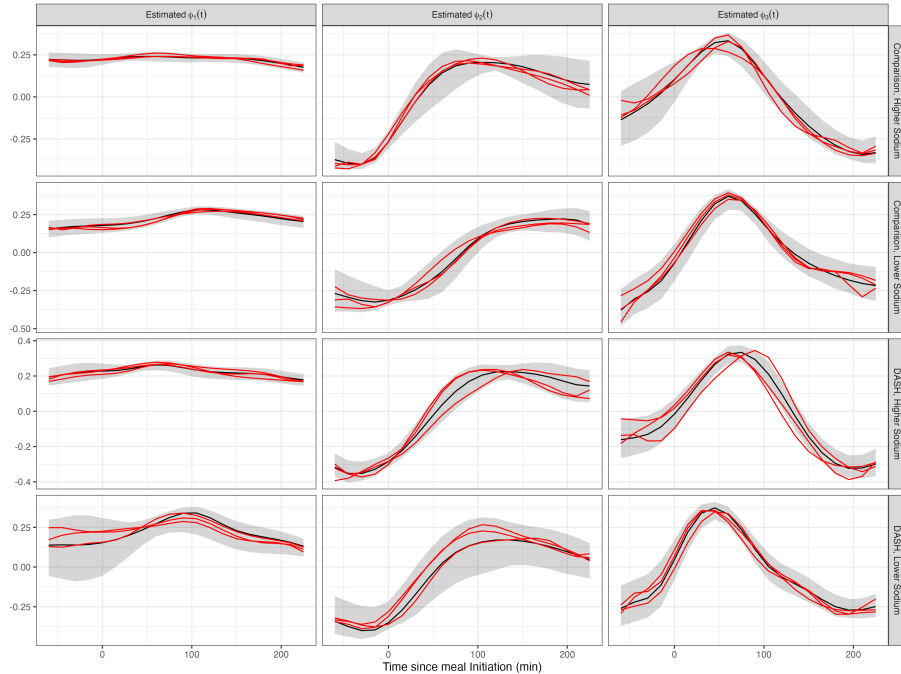


Figure S8: Bayesian FPCA results for the first three PCs (each column corresponds to one FPC) for each of the four diets (each row corresponds to one diet). X-axis: time from the start of the meal. Black curves: posterior mean; red curves: three samples from the posterior of the PCs; shaded areas: pointwise 95% credible intervals.

We present also the corresponding eigenvalues in Figure S9, where again one observes the uniqueness of the DASH, Lower Sodium diet. In this analysis as well, there is lower overall variability for this diet (assessed by sum of eigenfunctions). Further, this difference is again driven by the first eigenvalue/eigenfunction pair in this analysis.

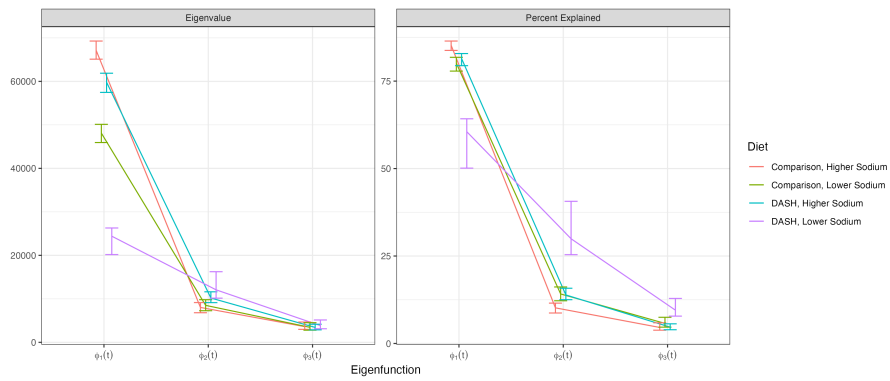


Figure S9: Eigenvalue and percent-variability estimates from the Bayesian FPCA models fit to each of the four diets (each line and color corresponds to one diet). X-axis: eigenfunction corresponding to eigenvalue/percent variance explained. All estimates are presented with their corresponding 95% credible intervals.

S5 Bayesian FPCA of average CGM within diets

In this section, we provide the monitoring figures produced to ensure that the analyses in Section 5.3 achieved convergence. Figures S10, S11, and S12 all present trace plots of the eigenfunction evaluations at particular points along the temporal domain ($t = 15, 105$ and 210 minutes relative to the start of the meal). These figures indicate effective mixing of the chains with minimal autocorrelation, providing evidence for convergence.



Figure S10: Trace plots displaying samples of $\phi_k(t)$ evaluated at $t = -45$ minutes relative to meal intake, where coloration indicates sampling chain

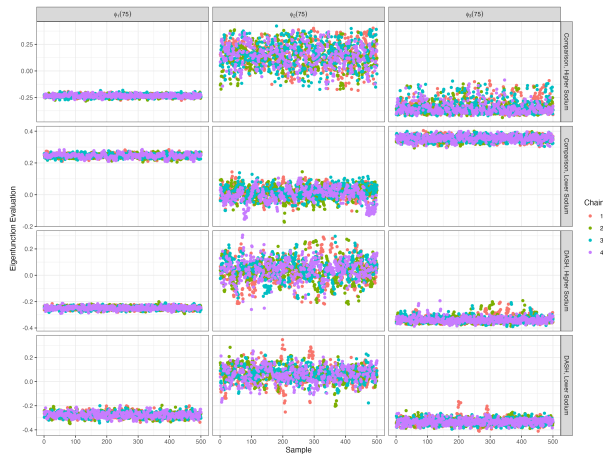


Figure S11: Trace plots displaying samples of $\phi_k(t)$ evaluated at $t = 75$ minutes relative to meal intake, where coloration indicates sampling chain.

We also visualized samples of the smooth curves at the data level in Figure S13. This figure was generated to assess whether our models represent the single-level data well throughout sampling. Figure S13 provides supporting evidence for this fact, as all raw data curves are approximated well by the smooth samples.

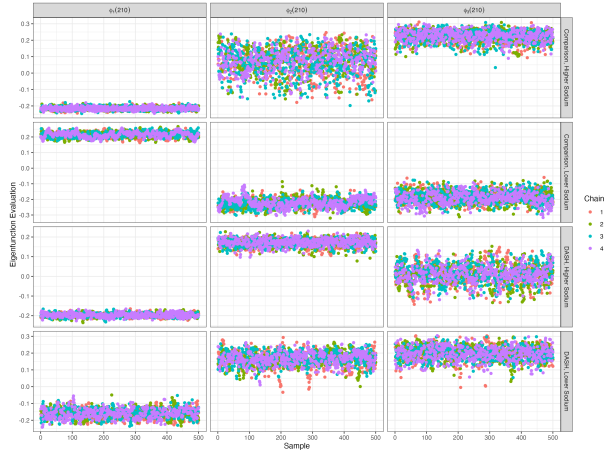


Figure S12: Trace plots displaying samples of $\phi_k(t)$ evaluated at $t = 210$ minutes relative to meal intake, where coloration indicates sampling chain

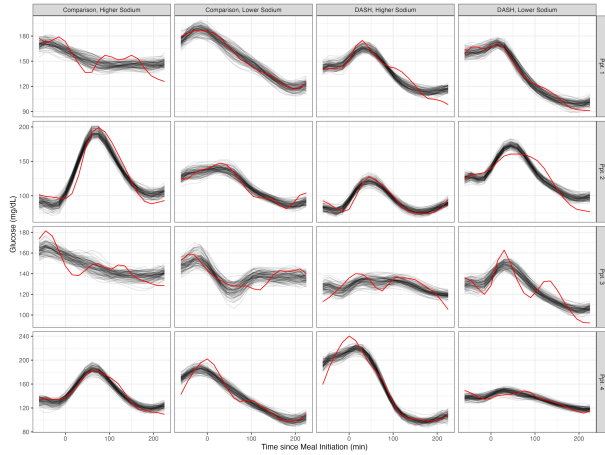


Figure S13: Visualization of samples from randomly selected underlying smooths $\hat{Y}_i(t) = \mu(t) + \sum_{k=1}^K \xi_{ik} \phi_k(t)$ from each FPCA model, with the original data $Y_i(t)$ overlaid. The black curves indicate samples, while the red curves correspond to the original data.

S6 Bayesian MFPCA of individual CGM curves

In this section, we provide the monitoring figures produced to ensure that the analyses in Section 5.4 achieved convergence. Figures S14, S15, and S16 all present trace plots of the eigenfunction evaluations at particular points along the temporal domain ($t = 15, 105$ and 210 minutes relative to the start of the meal). These figures indicate effective mixing of the chains with minimal autocorrelation, providing evidence for convergence.



Figure S14: Trace plots evaluating samples of $\phi_k^{(1)}(t), \phi_l^{(2)}(t)$ at $t = -45$ minutes relative to meal intake, where coloration indicates sampling chain.



Figure S15: Trace plots evaluating samples of $\phi_k^{(1)}(t), \phi_l^{(2)}(t)$ at $t = 75$ minutes relative to meal intake, where coloration indicates sampling chain.

We also visualized samples of the smooth curves at the data level in Figure S17. This figure was generated to assess whether our models represent the multi-level data well throughout sampling. Figure S17 provides supporting evidence for this fact, as all raw data curves are approximated well by the smooth samples.



Figure S16: Trace plots evaluating samples of $\phi_k^{(1)}(t), \phi_l^{(2)}(t)$ at $t = 210$ minutes relative to meal intake, where coloration indicates sampling chain.

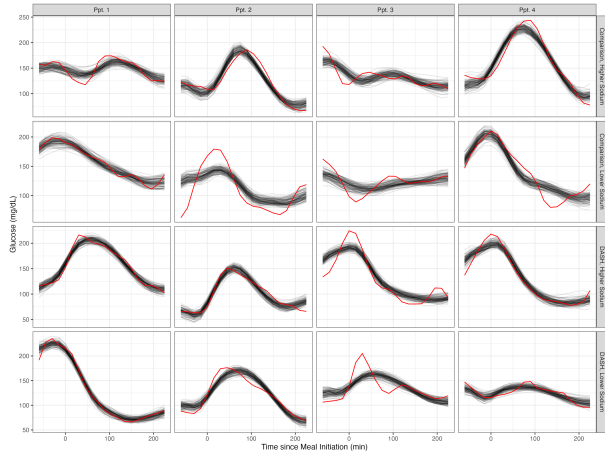


Figure S17: Visualization of samples from randomly selected underlying smooths $\hat{Y}_{ij}(t)$ from the fitted MFPCA model, with the original data $Y_{ij}(t)$ overlaid. The black curves indicate samples, while the red curves correspond to the original data.